Mixing and scalar dissipation rate statistics in a starting gas jet

N. Soulopoulos, Y. Hardalupas, and A. M. K. P. Taylor

Citation: Physics of Fluids **27**, 125103 (2015); doi: 10.1063/1.4935233
View online: http://dx.doi.org/10.1063/1.4935233
View Table of Contents: http://scitation.aip.org/content/aip/journal/pof2/27/12?ver=pdfcov
Published by the AIP Publishing

PHYSICS OF FLUIDS **27**, 125103 (2015)

Mixing and scalar dissipation rate statistics in a starting gas jet

N. Soulopoulos,[a] Y. Hardalupas, and A. M. K. P. Taylor
Mechanical Engineering Department, Imperial College London, SW7 2AZ London, United Kingdom

(Received 22 May 2015; accepted 26 October 2015; published online 9 December 2015)

We quantify the temporal development of the mixing field of a starting jet by measuring the mixture fraction and the scalar dissipation rate and their statistics in an isothermal, impulsively started, gaseous jet. The scalar measurements are performed using planar laser induced fluorescence and, with appropriate processing of the resulting images, allow scalar dissipation rate measurements within 20%. The probability density functions of the mixture fraction, measured within a region of the order of 3 times the Batchelor length scale of the flow, are bimodal and skewed around a well-mixed radial location, which depends on the downstream distance and the time after the start of injection. The instantaneous distributions of the scalar dissipation rate reveal regions of high mixing at the jet periphery and at the developing vortex ring. The normalised probability density function (pdf) of the scalar dissipation rate at various flow positions and times after the start of injection has the same characteristic shape but differs from the usually suggested lognormal distribution at both low and high dissipation values; the same, also, holds true for the pdf conditioned on different values of the mixture fraction. The mean of the scalar dissipation rate conditional on mixture fraction shows a variation across the mixture fraction range, which differs between flow locations and times after the start of injection; however, at later times and for larger downstream distances the conditional mean between flow locations has similar distributions. Implications of the measurements for the auto-ignition of gaseous jets are examined and demonstrate that near the nozzle exit or at earlier times conditions are un-favourable for auto-ignition. [http://dx.doi.org/10.1063/1.4935233]

I. INTRODUCTION

In contrast to the steady state gas jet, the starting gas jet has received less attention, despite its regular use in engineering, e.g., the gas injection in internal combustion engines. A starting jet is produced by suddenly injecting an amount of gas through a nozzle and allowing the jet to develop. At long times after start of injection (ASI), the starting jet becomes a well known steady state jet. However, in many applications the intermediate time behaviour of the flow is of primary importance. A characteristic feature of the starting jet is the head vortex, formed by the initial roll up of boundary layer vorticity inside the nozzle, as the gas is injected into an otherwise quiescent environment.[1] A model used to study the evolution of the starting jet[2] relies on the assumption that the head vortex grows by entraining jet fluid only and for long times ASI, the model agrees reasonably with measurements.[3] For intermediate times ASI this is not actually true and entrainment of ambient fluid does take place through the vortical motion of the head vortex.[4] However, for even earlier times ASI, there is evidence that there is limited entrainment of ambient fluid into the head vortex.[5] The large scale entrainment of ambient fluid and potential differences with steady state behaviour is

[a]Electronic mail: ns6@ic.ac.uk

an important consideration in the mixing of unsteady jets, since the probability density function of a passive scalar quantity will be most influenced by these large scale vortical motions.

A characteristic time scale describing the evolution of the starting jet is $T = D/V$, where D and V are the nozzle exit diameter and the injection velocity, respectively. In many experiments and calculations the injection profile, i.e., the time variation of the injection velocity, is considered as being nearly top-hat and this is the assumption in the following discussion and in the presented experiments. Qualitatively, a low T implies a quick interaction of the emerging jet with its surroundings, which leads to slower approach to a semi-steady state, whereas a higher T signifies larger jet inertia. A range of characteristic time scales has been reported in experiments and calculations, from 10^{-3} ms to ~1 ms. The starting jet reaches its semi-steady state at non-dimensional times[3,6] $t_* = \frac{t}{T} > 100$, whereas a transient period in the jet development exists for $t_* \sim 20$ at a non-dimensional axial distance[7] $x_* = x/D \approx 10$ (x being the downstream distance from the nozzle exit). For the earlier times after the start of injection, e.g., $t_* < 20$, the head vortex seems to grow by entraining fluid from the jet axis, rather than its surroundings,[5,6] but at locations upstream of the head vortex the jet body interacts with its surroundings and entrains ambient fluid. At later times, $t_* > 70$, the head vortex entrains ambient fluid and the overall entrainment of the starting jet is larger than the corresponding entrainment of a stationary jet.[7,8] In fact, the developing vortex ring is very efficient in growing its circulation and entraining ambient fluid until the time where a trailing jet appears behind it. Past this stage, nozzle, rather than ambient, fluid feeds the development of the vortex ring. The so-called "formation number"[9] provides the time beyond which a vortex ring stops being very efficient in entrainment and its value has been established in experiments[9] and calculations[10] as $t_* = 3 \sim 4$; alternatively the formation number describes the effective stroke ratio of a given injector, L/D (where L is the effective stroke length, defined as the time integral of the exit velocity profile[9,10]).

It is instructive, also, to consider any relation between a starting gas jet and a spray, since this can allow a qualitative transfer of insight into a combustion engine scenario. Before a starting jet reaches its semi-steady state, at $t_* = 20$–30, a similarity exists between a gaseous jet and a spray along rays of constant angle emanating from the origin at a proper non-dimensional time.[7] At equivalent $x_* = \frac{x}{y}$ (x, y are the axial and radial coordinates from the centre of the nozzle, respectively) and $t_* = \frac{V_v}{V_0}\frac{t/T}{y/D}$ (V_v is the head vortex convection velocity) the entrainment characteristics are similar between gaseous jets and diesel sprays, where the density difference between injected and ambient fluids enters the description through the dependence of V_v on the density ratio. In terms of the formation number, typical jet and spray flows have different values for the maximum effective stroke ratio: gas jets[3,7] (including the present experiments) have $L_{\max}/D \sim 10^2$ and typical diesel sprays have $L_{\max}/D \sim 10^3$. This implies that gas jets will achieve a level of entrainment faster, i.e., in fewer nozzle diameters downstream, than diesel sprays.

In a two-stream mixing situation, including cases with reaction, the mixture fraction (ζ) is a conserved scalar and defines the fraction of the local mixture that originates from the fuel stream. In frozen mixing and during combustion, mass fractions and temperature are functions of the mixture fraction and this functional dependence holds in both laminar and turbulent flows; in the latter case the probability density function (pdf) of the mixture fraction accounts for the effect of turbulent fluctuations. The pdf of ζ quantifies large scale mixing between the fluids and directly affects the small scale distributions of the scalar field.[11] The pdf is, also, used to predict species concentrations and temperature, for example, the concentration in isothermal flows uses the pdf of ζ and many combustion models of turbulent non-premixed combustion use it in some way.[12] Qualitatively, the pdf of ζ can, additionally, point to unexpected mixing influences, such as flow flapping.

At the smallest turbulent scales, the scalar dissipation rate (χ) and its pdf quantify the extent of molecular mixing; χ is a fundamental quantity in turbulence[13] and ubiquitous in combustion modelling.[12] A more complete description, however, of turbulent mixing involves the joint pdf (jpdf) of mixture fraction and scalar dissipation rate, which serves, among other things, to account for finite rate chemistry effects in a flamelet description of turbulent non-premixed combustion. A common assumption is that the mixture fraction and its scalar dissipation rate are statistically independent, so the jpdf is the product of the individual pdf, i.e., $p(\zeta, \chi) = p(\zeta)p(\chi)$. Usually, further assumptions

on the shape of the individual pdf allow estimates to be made and common shapes are the β-pdf for the mixture fraction and a lognormal pdf for the scalar dissipation rate.

The average of the scalar dissipation rate conditional on different values of the mixture fraction allows one to focus the description of mixing and combustion along particular flow areas (i.e., iso-contours of the mixture fraction), where more rigorous mixing or actual combustion might take place. The conditional mean of the scalar dissipation rate, $\langle \chi | \zeta = \zeta^* \rangle$ (for simplicity $\langle \chi | \zeta \rangle$), appears in many models of turbulent non-premixed combustion and, also, in the general approach of the transport equation for the pdf of mixture fraction. In fact, weighing the conditional mean with the probability that it might occur, i.e., the product $\langle \chi | \zeta \rangle \, p(\zeta)$, is widely encountered during estimates and in modelling attempts.

Several experiments were performed to measure the statistics of a passive scalar and its dissipation rate in isothermal and reacting flows and results from isothermal experiments can provide insights on the physics of non-premixed flames.[14] The shape of pdf (ζ) can determine not only the large scale mixing but also the joint statistics of a passive scalar and its dissipation, including the conditional dissipation. A gaussian pdf, as measured in isothermal boundary layer and jet flows,[15] results in conditional dissipation, which is independent of the underlying scalar. This result is also theoretically verified[16] to show that if the pdf is not gaussian, there is a dependence of the dissipation rate on the scalar. However, it is not just the symmetry of the gaussian pdf that causes the independence of the dissipation on the scalar. In cases where bimodal pdf have been measured[17] or used in calculations[18] they reveal insightful flow characteristics and in such cases the conditional dissipation shows a strong dependence on the underlying scalar. Even though the focus of the present work is on shear flows, we mention that symmetric scalar pdf with exponential tails, measured in grid turbulence,[19,20] result also in a non-linear dependence between a passive scalar and its dissipation. The effect of the tails of the ζ pdf on the conditional statistics is, also, noticed in a variety of shear flows, such as wakes, jets, and boundary layers,[21] where it is suggested that stretched tails result in peaks of the conditional dissipation distribution. The above observations are corroborated by additional measurements in boundary layers,[15] jets,[15,22,23] opposed flows,[24] and in calculations.[25] The same picture emerges from measurements in non-premixed reacting flows. In these cases, the shape of the pdf of the mixture fraction determines the dependence of the dissipation on the scalar. For example, in various experiments,[24,26–29] the conditional dissipation shows a dependence on the mixture fraction. Similarly to the conditional dissipation, statistical independence between the scalar and its dissipation depends on pdf (ζ). In cases where the scalar pdf is gaussian and the scalar-dissipation rate correlation is zero, as in the far downstream region of an isothermal jet,[22] statistical independence between the two holds; however, for non-symmetric scalar pdf[15,17] statistical independence is not valid.

The pdf of the (conditional) scalar dissipation rate has been largely assumed to follow a lognormal distribution, whose mean and variance enter in models of turbulent combustion. However, many measured pdf (χ) show a difference to the lognormal distribution at both low and high values of χ in isothermal[17,30–32] and reacting flows.[24,27–29] The pdf typically has longer tails for low dissipation rate values and falls-off faster at high dissipation rate values, compared to the lognormal distribution. Whether this effect depends on the dimensionality of the measurements, the spatial resolution, the measurement noise, or it is an inherent feature of the dissipation pdf is not entirely clear. For example, by assuming an isotropic small scale field, lower dimensional measurements of the dissipation can be reconstructed to provide the pdf of a full 3D measurement,[33] which is shown to follow closely a lognormal distribution.

Whereas there exist data on the velocity field development of the starting jet, there seem to be even fewer studies concentrated on the scalar field; at the same time, small scale scalar measurements are almost entirely performed in steady flows. The effect of the unsteady, early stage development on the large and small scales mixing remains somehow unknown but can shed light on the characteristics of turbulence in this setting and corroborate the understanding and control of engineering devices, such as automotive gas injectors and possibly diesel injectors. So, the objective of the present work is to contribute towards this goal by providing mixing and dissipation rate field data on an unsteady gaseous isothermal jet. The rest of the paper is structured as follows: Sec. II describes the experimental arrangement of the unsteady jet, Section III presents the mixture

fraction field and its statistics, and Sections IV and V present the scalar dissipation rate field and its unconditional and conditional statistics and the paper concludes with a summary.

II. FLOW ARRANGEMENT AND MEASUREMENT METHOD

The experimental configuration for the measurement of the mixing field of an unsteady gas jet consists of the flow setup, the optical technique, and the data processing methodology.

A fast acting, automotive-type gas injector (KEIHIN KN3-2B) injects the starting jet, issued inside a 30∗30 cm^2 enclosure. A very slow co-flow—conditioned with several wire screens, a porous plate and a honeycomb—is established inside the square test section in order to carry the injected fluid and acetone towards the lab's exhaust system. The injector's solenoid valve is placed 20 mm upstream of the $D = 4$ mm nozzle internal diameter, with a nozzle lip thickness of about 1 mm. The valve opening time is ∼1 ms, the injection duration is 10 ms and the injection velocity averaged across the nozzle area is $u = 20$ m/s, as determined by the manufacturer's mass flow rate data and the constant 2.5 bar back pressure. These values result in a Reynolds number of 4500 and a characteristic time scale $T = d/u = 0.2$ ms. The jet fluid is air seeded with acetone vapor and exits the injector at 65 °C. Upstream of the enclosure, conditioning sections create a low turbulence heated air co-flow with a velocity of 0.1 m/s; the temperature inside the enclosure is, also, kept at 65 °C ± 7 °C. Figure 1 shows the flow arrangement.

Planar Laser Induced Fluorescence (PLIF) of acetone is used to measure the jet fluid concentration across a plane encompassing the nozzle centreline, using the fourth harmonic of a pulsed Nd:YAG laser at 266 nm and a 16-bit Intensified CCD (ICCD) camera. Three cylindrical fused silica lenses generate a laser sheet 45 mm high and 130 μm thick, with 100 mJ/pulse energy at the measurement area. A beam splitter placed just before the enclosure reflects 5% of the laser light into a dye cell containing a solution of Rhodamine 6G. A camera captures the emitted fluorescence signal to monitor the laser energy and sheet profile on a shot-by-shot basis. The ICCD camera (Andor DH534-18F-03) is fitted with a 50 mm, f#1.2 (f# is the lens f-number) Nikkon lens and a 13 mm extension ring. A BG-3 (Schott) colour filter rejects light at the laser wavelength and allows the fluorescent light at the blue region of the spectrum to pass through. A plan view of the optical setup is given in Figure 2.

The intensity of the captured acetone fluorescence signal varies linearly with the local concentration of the acetone vapour, following appropriate image corrections for the laser sheet profile and energy, the camera background, and dark signals and ensuring an adequate flat field response of the camera. In turn, the local acetone vapour signal is also linearly related to the concentration of the jet fluid at the same location. By normalising the acetone fluorescent intensity by the fluorescent intensity signal at the nozzle exit, within the potential core of the jet (which is captured at all images), we arrive at the local mixture fraction of the jet fluid. The nozzle exit fluorescent intensity signal

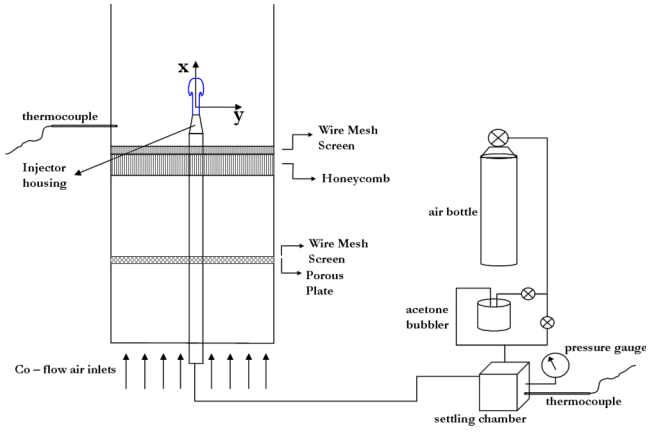

FIG. 1. The experimental arrangement and the coordinate system used.

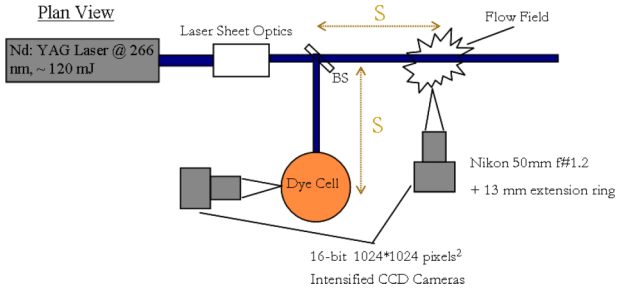

FIG. 2. Plan view of the optical setup.

remains within 3% between different instantaneous images and the absorption of the laser light along its propagation direction, and within the potential core, is around 2%, meaning that relatively little laser absorption takes place. The field of view of the measurements (46∗46 mm^2) captures the whole spatial variation of the instantaneous mixture fraction distribution and the temporal variation is gauged through ensemble averaging of instantaneous images at the same time ASI. Between 300 and 500 instantaneous images are acquired at every ASI, which are t/T = 0.9, 2.15, 3.4, 4.65, 5.9, 7.15, 9.65, 10.9, 13.4, 15.9.

Using the instantaneous mixture fraction distributions, the scalar dissipation rate is $\chi = \mathfrak{D}\left[(\partial\zeta/\partial x)^2 + (\partial\zeta/\partial y)^2\right]$, using the projection of the scalar gradient in 2 dimensions (where $\mathfrak{D}$ is the diffusivity). The gradient calculation follows from second order numerical differentiation, i.e., $\partial\zeta/\partial x = \left(\zeta_{i+1,j} - \zeta_{i-1,j}\right)/(2\Delta x)$, where Δx is the pixel size and $\zeta_{i+1,j} = \zeta(x + \Delta x, y)$. The choice of the differentiation scheme depends on the resolution and signal-to-noise ratio (SNR) of the measurements. While a higher order differentiation scheme has better spectral response, its outcome depends on the relative length scales between the scalar structure and the spatial resolution. We, also, used a scheme that rotates the pixel array by 45°and calculated the derivative as an average of the original and rotated fields and the resulting difference in the mean scalar dissipation rate is less than 2% from the values obtained through 2nd order differencing.

The measurement spatial resolution affects directly the accurate calculation of the scalar dissipation rate. We quantify the spatial resolution with the Point Spread Function (PSF) of the imaging system,[34] which we calculate using a scanning knife edge technique: the full width at half maximum of the resulting PSF is 0.24 mm. The smallest scalar spatial length scale is the Batchelor length scale, $\eta_B = \eta Sc^{-1/2}$, where η and Sc are the Kolmogorov length scale and the flow Schmidt number, respectively. In the present experiment $Sc = 1$, so the Batchelor and Kolmogorov length scales are equal. We use the scalar dissipation power spectrum to estimate the Batchelor length scale and set it at the wavenumber where the dissipation spectrum is at 2% of the peak value.[35] The Batchelor length scale varies with flow location and time ASI from 250 μm to 320 μm, and we set $\eta_B = 250$ μm. The scalar power spectra are also used to determine the SNR of the measurements, which is always SNR > 50 and typically SNR ≈ 100.

Finally, experimental noise is also detrimental to the calculation of the dissipation rate. We treat its effect by using the Wiener filter, taking into account the PSF of the imaging system, which accounts, also, for the blurring due to spatial resolution. This procedure allows the reconstruction of the uncorrupted signal and the calculation of the accuracy of the resulting scalar variance and scalar dissipation rate. The errors in the determination of the scalar variance range, depending on the time ASI, from 1% to 3.5% and the errors in the dissipation rate range from 10% to 29%, with the average error being within 20%. More details on the experimental setup, the data processing and the error assessment are provided in Ref. 36.

III. AVERAGE AND FLUCTUATIONS OF THE MIXTURE FRACTION

A. Instantaneous and ensemble averaged mixture fraction

Sample instantaneous mixture fraction images at various times after the start of injection are shown in Figure 3. As the jet fluid exits the nozzle, the boundary layer from the wall of the nozzle

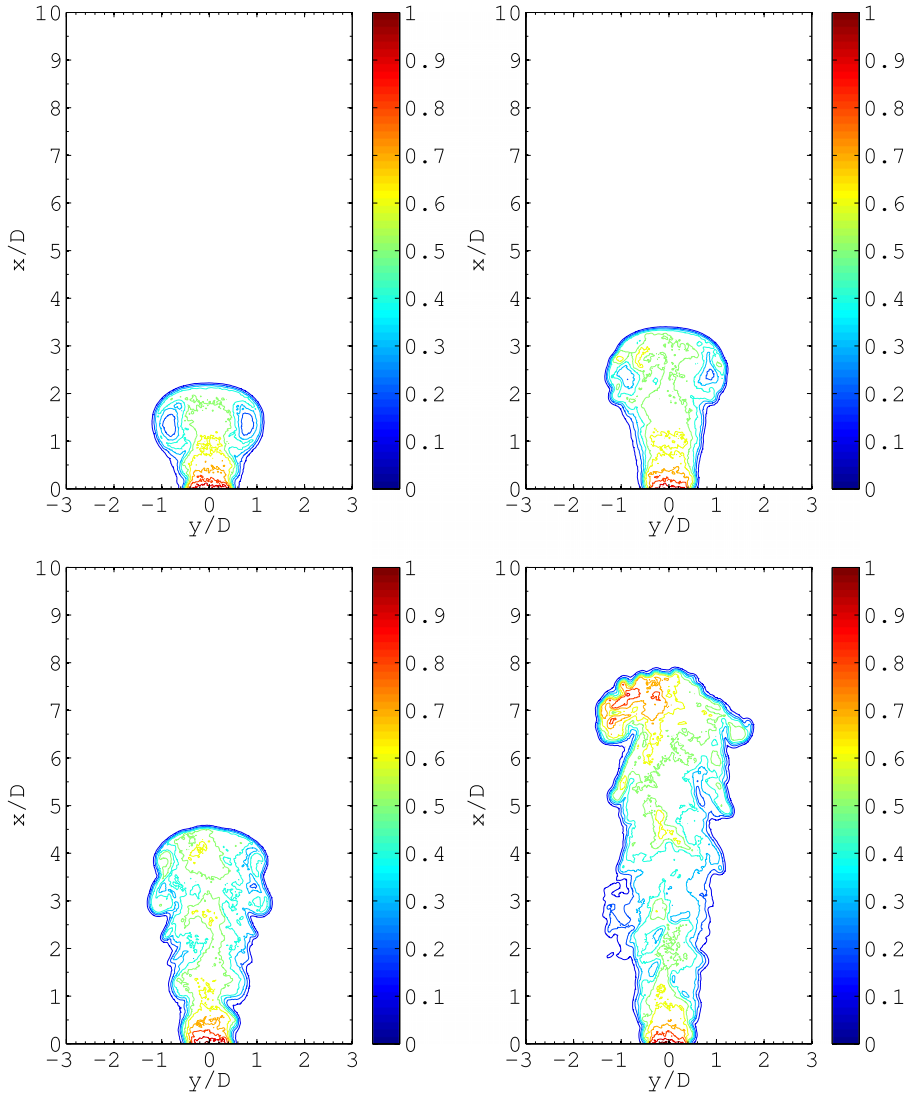

FIG. 3. Sample instantaneous images of mixture fraction at various times after the start of injection. From left to right and top to bottom, t/T = 3.4, 7.15, 9.65, and 15.9.

separates and forms a vortex sheet. Subsequently, this vortex sheet rolls up, entrains ambient fluid and forms a vortex ring. This mushroom-like structure is observed in the instantaneous images of Figure 3 for the earlier time (t/T = 3.4) and is seen to persist until t/T = 7.15, whereas for later times the distinctive core of the vortex ring seems to disappear. As the injection event continues, a trailing jet is formed behind the developing vortex ring. At earlier times ASI, the vortex ring is the main mechanism by which ambient fluid is entrained and mixed with jet fluid, since no large scale structures are evident in the trailing jet. Later than t/T ≈ 7 indentations start to appear at the sides of the jet, which grow in size and allow further engulfment of ambient fluid. The entrainment of ambient fluid at the earlier times, until t/T = 7.15 at 4 nozzle diameters downstream, is confined to the core of the vortex ring and to a thin region at the boundaries of the jet; the main body of the jet consists of very rich jet fluid with mixture fraction values, typically, more than 0.7. At the instantaneous image at t/T = 15.9 in Figure 3 values of the mixture fraction larger than about 0.6 are found at the leading edge of the jet, whereas the main body of the jet has been diluted with ambient fluid to mixture fraction values of 0.2–0.5. It is interesting to note that even at the last acquired time high values of mixture fraction are still found at the leading edge of the jet; in a steady

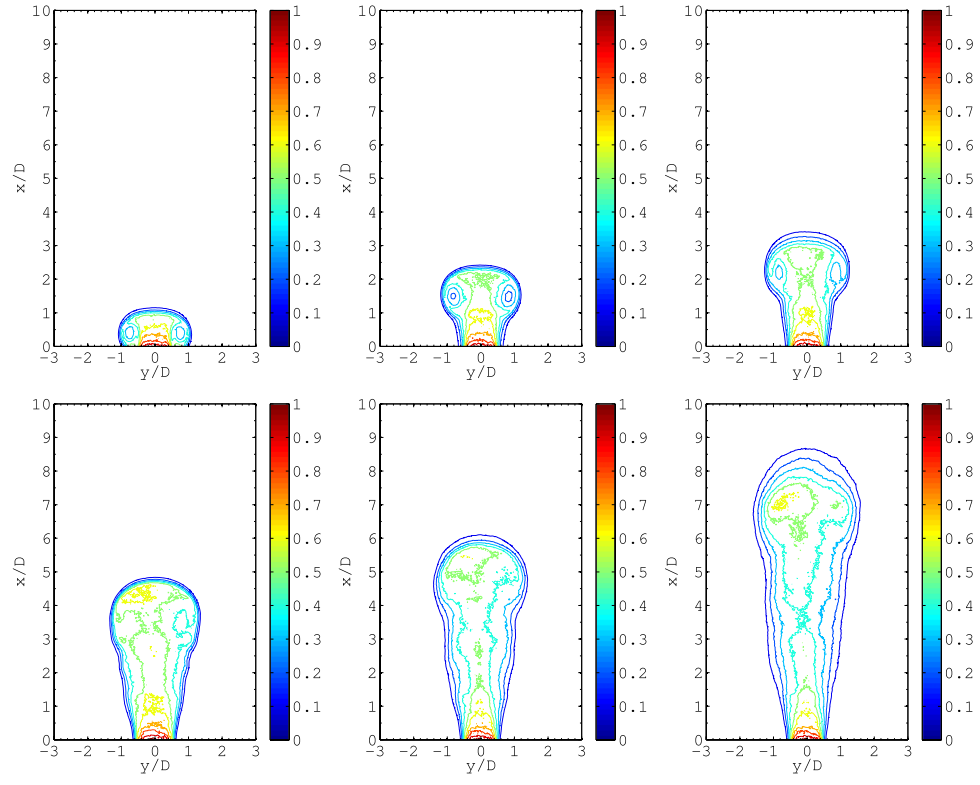

FIG. 4. The mean mixture fraction field at times t/T = 2.15, 4.65, 7.15, 9.65, 10.9, 13.4. Time increases from left to right and top to bottom.

jet, in contrast, it is unlikely to find large mixture fraction values at such distances downstream of the nozzle exit. Some implications of this distinct mixing characteristic of the starting jet will be explored further when the conditional statistics of the scalar dissipation rate will are presented.

The mean mixture fraction field and the standard deviation of the mixture fraction fluctuations for different times after the start of injection are shown in Figures 4 and 5, respectively. At the earlier times until t/T = 10, in agreement with the instantaneous images, the vortex ring is well defined while, around the circulating core, the jet fluid is more diluted than within the jet body. For these earlier times, (t/T = 0.9–5.9, up to 5 nozzle diameters downstream), the standard deviation of the mixture fraction is about 10% of the mean for most of the jet. The largest values of standard deviation are concentrated at the boundaries and at the leading portion of the jet. At these positions the mixture fraction fluctuations can be as high as 100% of the local mean value. Instead, at the main body of the jet, especially for the earlier times, the mixture fraction fluctuations are minimal indicating the lack of ambient fluid entrainment. The area occupied by large mixture fraction fluctuations is broadened axially around the head vortex at later times and the level of the fluctuations increases, reaching 20%–25%, in contrast to the main jet body where the fluctuations do not generally exceed 10%–15% of the mean. With increasing time, later than t/T ≈ 10, the vortex ring pinches-off the main jet body and continues to propagate downstream, whereas in the upstream region the jet starts to assume a semi-steady condition (which is not, however, fully established before the last time ASI acquired).

The instantaneous mixture fraction distributions are processed in order to extract structural characteristics of the developing jet, such as the penetration length. A cross section average mixture fraction is calculated at every downstream distance and the axial location at which this average falls below a threshold level is defined as the penetration length for the particular instantaneous flow realisation. The selected threshold level is 0.02 mixture fraction units. However, changing this level by ±0.01 leads to the penetration length varying within ~0.2 mm. This procedure is

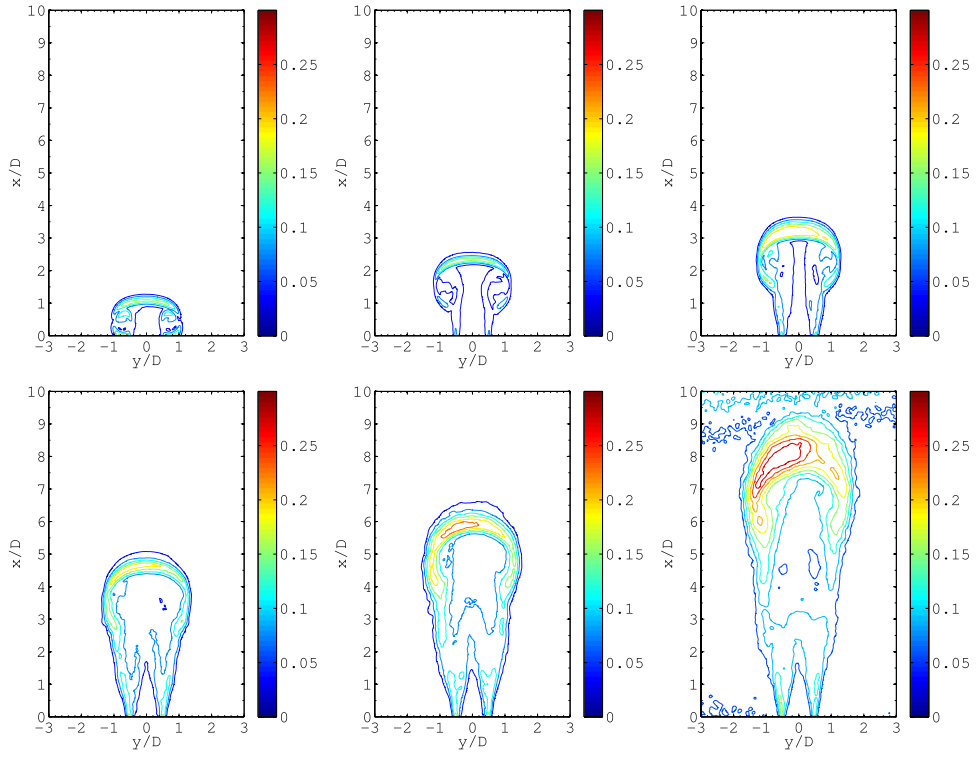

FIG. 5. The standard deviation of the mixture fraction fluctuations at times t/T = 2.15, 4.65, 7.15, 9.65, 10.9, 13.4. Time increases from left to right and top to bottom.

repeated for every image at all time instants, so the ensemble mean and standard deviation of the penetration length are calculated. Figure 6 shows the penetration length as a function of time after the start of injection, where the error bars represent one standard deviation above and below each point, along with a linear fit to the first 9 data points. A linear trend in the penetration distance with respect to time ASI was observed in other experiments and calculations[5] of starting jets, for non-dimensional times $t/T < 10$. The jet tip penetration velocity, defined as the slope of the linear fit, is $u_{\text{tip}} = 9.90 \pm 1.25$ m/s, which is about half the jet injection velocity.[5,37] The same threshold level is used to identify the instantaneous contour of the jet. In this way, the vortex ring is identified as the maximum width of the jet at every time instant. Similarly to the jet penetration, the vortex ring also grows linearly with time and expands radially at a rate of $u_{\text{ring}} = 1.47 \pm 0.3$ m/s.

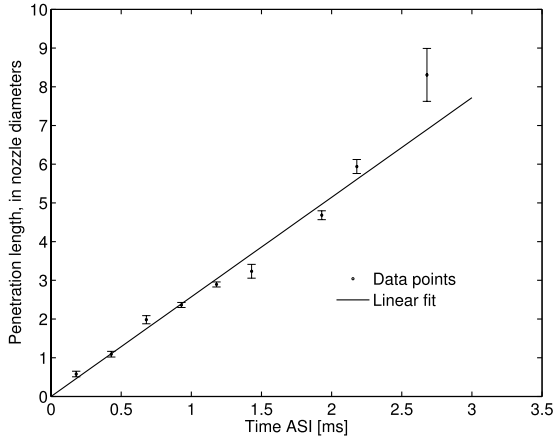

FIG. 6. The penetration length as a function of the time ASI and a linear fit to the data.

The development of the mixture fraction field of a starting jet for times until t/T = 15–20 shows differences to the steady state jet, most notably the large gradients and corresponding (apparent) large fluctuations at the periphery of the jet and in the leading edge, the propagation of largely unmixed jet fluid to the downstream location of the vortex ring, and the detachment of the vortex ring (in this case at t/T ≈ 10). The semi-steady state seems to take place at similar, albeit somehow earlier, times ASI as in previous studies (later than t/T = 15–20). Some of the implications of these mixing characteristics will be explored further in Sec. III B and when discussing the statistics of the scalar dissipation rate field.

B. Probability density functions of the mixture fraction

Estimates of the pdf of the mixture fraction at a spatial location and time ASI are calculated by considering the mixture fraction values from all instantaneous images within a square window of side 1 mm by 0.7 mm in the axial and radial directions, respectively, so the pdfs are constructed using more than 10^5 values. This area corresponds to $\sim 3 \times 4$ times the Batchelor length scale and was chosen as a compromise between locality of the pdf and statistical convergence of the sample. For an axial distance near the nozzle exit, x/D = 2 in Figure 7, the pdfs are nearly gaussian at the jet centreline (i.e., the leftmost column in the figure), but only for early times ASI. Even for this short distance downstream of the nozzle exit, the mixture fraction has assumed a mean value of ~0.5 as a result of the entrainment of ambient fluid from the vortex ring. Later on, the peak mixture fraction does not change at this location and a spread of mixture fractions to lower values is observed, which becomes more pronounced as time advances. This could be due to the increasingly larger indentations appearing as the jet develops, observed at the instantaneous distributions in Figure 3, which become of such size as to reach the jet centreline.

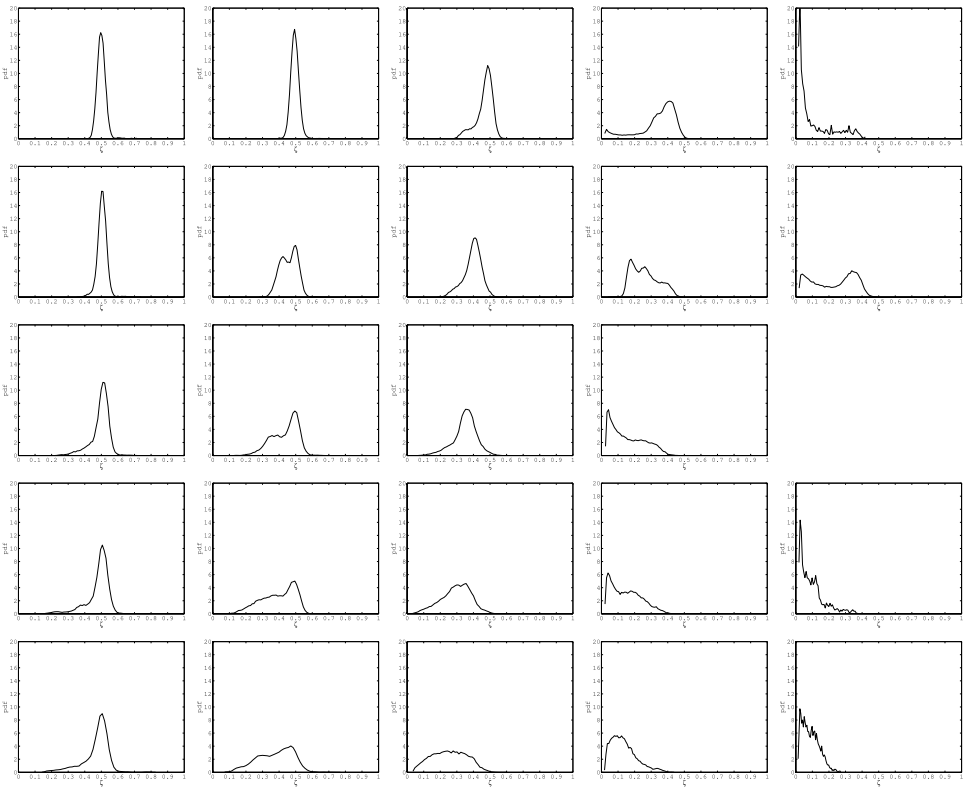

FIG. 7. The probability density functions of mixture fraction at x/D = 2 and, from left to right, y/D = 0, 0.3, 0.6, 0.9, 1.2. The time ASI increases from top to bottom, t/T = 4.65, 7.15, 9.65, 10.9, 13.4. Moving along a row in this figure shows the pdfs at increasing radial distances from the centreline.

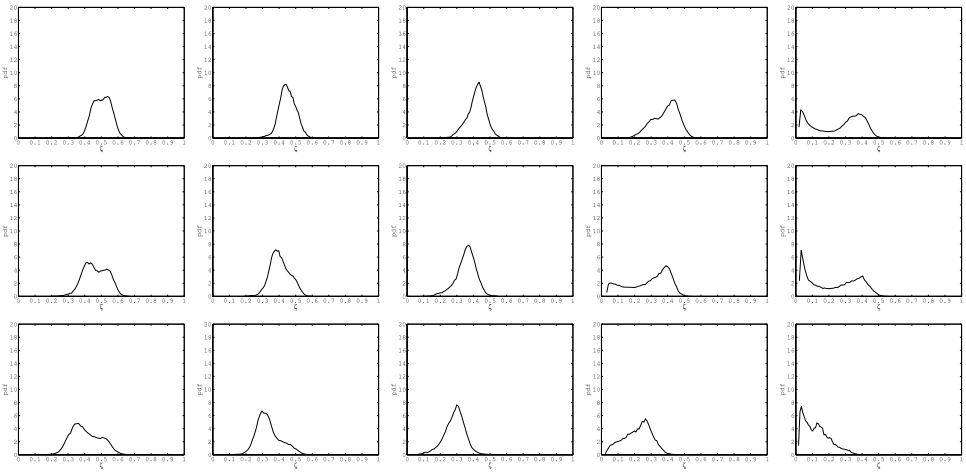

FIG. 8. The probability density functions of mixture fraction at x/D = 4 and, from left to right, y/D = 0, 0.3, 0.6, 0.9, 1.2. The time ASI increases from top to bottom, t/T = 9.65, 10.9, 13.4.

Moving along the radial direction at time t/T = 7.15 (i.e., along the second row in Figure 7) the pdfs at y/D = 0.3 and y/D = 0.9 (the second and fourth plots) are bimodal but having reversed relative peaks; at the same time, the pdf at y/D = 0.6 shows a single peak, albeit being somehow skewed towards lower values. At later times ASI, the bimodality of the pdf, at the same radial location, is reduced and the magnitude of the peaks also reduces, while the pdfs become flatter. At the near-centerline position, y/D = 0.3, the peak value is ~0.5 and lower values become more common with increasing time. The opposite is true at y/D = 0.9, where ambient fluid is mostly present, with less frequent encounters of jet fluid. In between these two locations, at y/D = 0.6, we find fluid with increasingly broader range of mixture fraction values, as the time ASI advances; the mean value decreases with time as more ambient fluid is mixed with jet fluid. These radial distances are located around the shear layer of the developing jet, where large scale intermittency results in the observed behaviour. It is, also, interesting to note that at y/D = 1.2 there are frequent occurrences of relatively unmixed jet fluid at earlier times, which disappear at a later stage; the passage of the vortex ring can explain, for example, the values of $\zeta \sim 0.4$ at y/D = 1.2 and t/T = 7.15.

At a further downstream distance, x/D = 4 in Figure 8, we, also, observe initially bimodal and progressively broad and skewed pdfs with a "reversal" of the peak between radial distances y/D = 0.9 and y/D = 1.2 (the last two columns in the figure). At both locations and with increasing time, the peak value of the pdf at y/D = 0.9 decreases from ~0.45 to ~0.3, whereas at y/D = 1.2 the peak at large ζ, ~0.4, disappears at later times. At x/D = 6 and x/D = 8, Figures 9 and 10, we observe similar trends, predominantly high (y/D = 0.9) or low(y/D = 1.2) values of mixture fraction, but with either a bimodal or broad distribution. It is, finally, interesting to note that at the

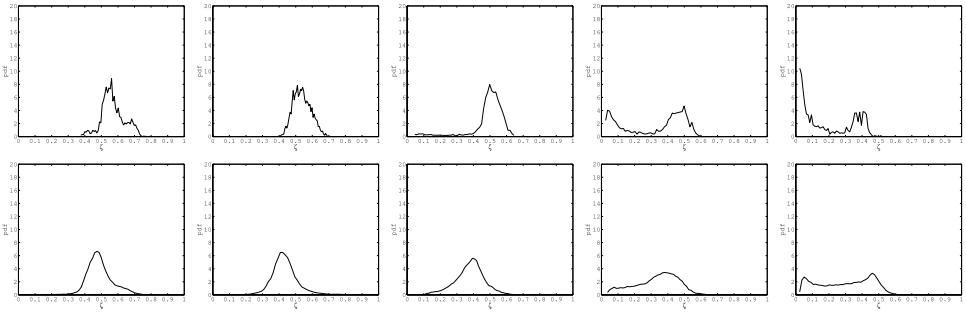

FIG. 9. The probability density functions of mixture fraction at x/D = 6 and, from left to right, y/D = 0, 0.3, 0.6, 0.9, 1.2. The time ASI increases from top to bottom, t/T = 10.9, 13.4.

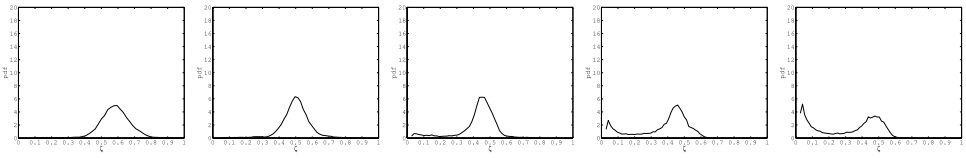

FIG. 10. The probability density functions of mixture fraction at x/D = 8 and, from left to right, y/D = 0, 0.3, 0.6, 0.9, 1.2. The time ASI is t/T = 13.4.

centreline at x/D = 4 and x/D = 6, the pdfs of ζ, also, assume a broad and even bimodal distribution, with increasing time; the peaks of the distributions move to lower mixture fractions as time ASI increases. Again, the large scale flow structures formed near the end of the injection upstream of the jet leading edge allow mixing of ambient and jet fluids at locations that would not otherwise been possible.

The skewness and kurtosis conveniently quantify some of the features of the pdfs, presented above, as follows. Positive skewness means that fluctuations of mixture fraction are more likely to take on large positive values than large negative values, indicating that there is a relatively long 'tail' of fluctuations in mixture fraction above the mean: thus there are relatively infrequent bursts of positive fluctuations in zeta. The magnitude of the kurtosis quantifies the extent to which the tail is relatively long. A gaussian distribution has skewness equal to zero and kurtosis equal to three.

Cursory inspection of the centreline, and one near centreline, pdfs at x/D = 2 for t/T = 4.65, 7.15, Figure 7, suggests the existence of a gaussian-like distribution. However, the magnitudes of the corresponding skewness and kurtosis (Figures 11 and 12) show that this is far from being the case and close inspection of Figure 7 reveals the existence of a long, but low probability, tail on the positive side of the distribution. In other words there remain incursions of relatively unmixed nozzle fluid at this location and at these early times ASI, albeit very infrequently. With increasing time, the skewness changes sign and the kurtosis becomes smaller, corresponding now to more frequent incursions of leaner than average tails. In the corresponding radial profiles of skewness, the rapid change in the sign, as well as the magnitude, reflects the transition from the pseudo-Gaussian on

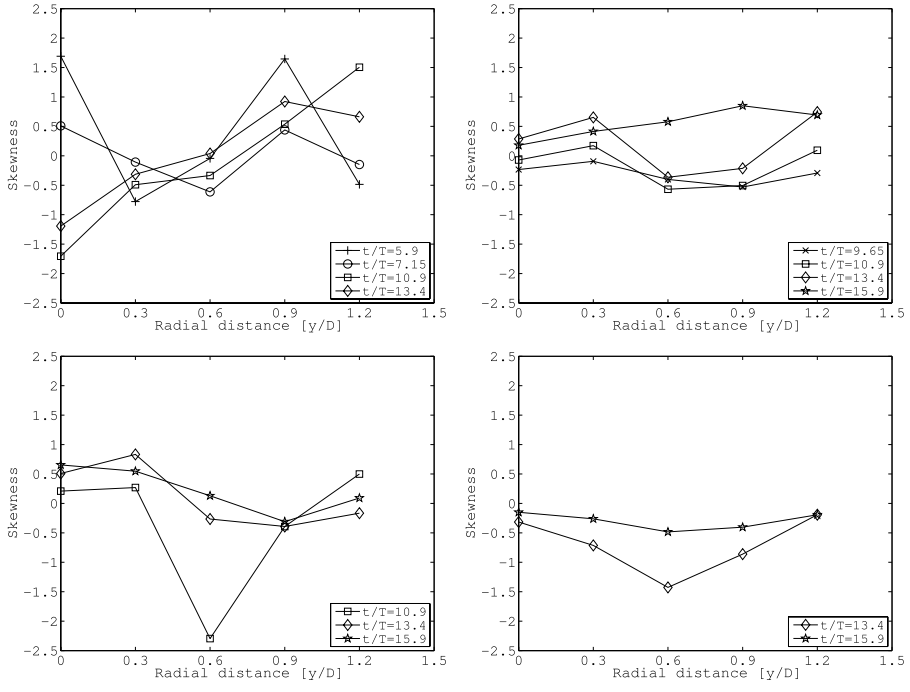

FIG. 11. The radial distribution of the mixture fraction skewness at different times ASI. The axial distance is x/D = 2, 4, 6, 8, from top to bottom and left to right.

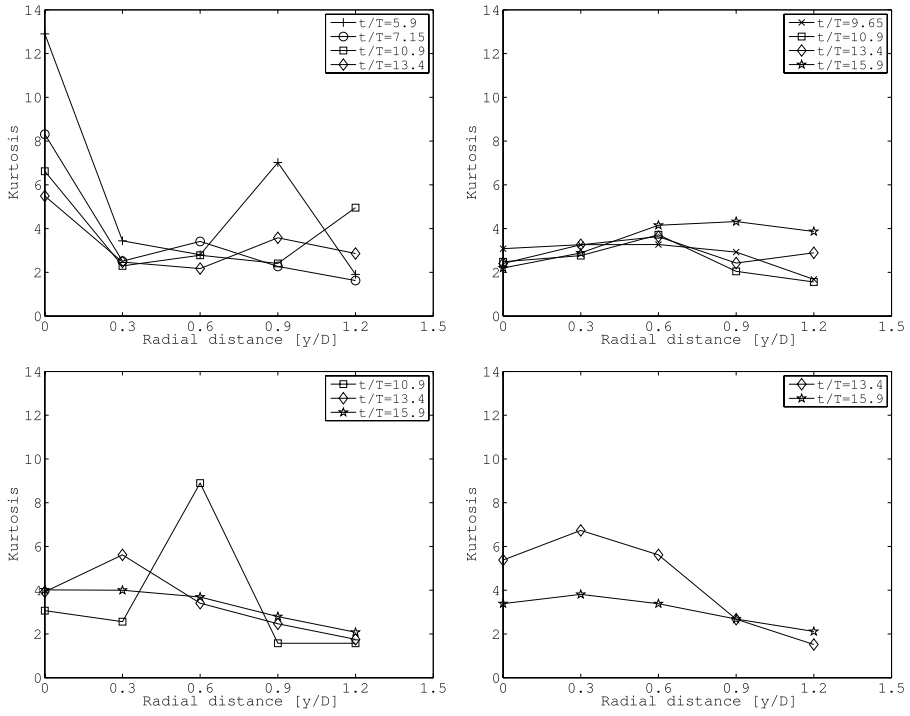

FIG. 12. The radial distribution of the mixture fraction kurtosis at different times ASI. The axial distance is x/D = 2, 4, 6, 8, from top to bottom and left to right.

the centreline through the bimodal to the negatively skewed shape at the edge of the jet. As an aside, it is worth noting that although the kurtosis falls to near Gaussian levels with increasing radial distance, the shape of the profiles is anything but Gaussian.

At x/D = 4 and near the centreline, Figure 11, the skewness changes sign with time, reflecting the otherwise unremarkable temporal development of the weakly bi-modal pdf shape: with increasing radial distance, strong bimodal profiles arises, with however surprisingly little qualitative change in the magnitude in the skewness to accompany this. The clustering of the kurtosis around a value of about 3 ± 1 reflects not a Gaussian-like distribution but rather compact distributions clustered relatively closely to the mean. These relatively featureless radial profiles are also seen for x/D = 6 and 8, Figures 11 and 12, with notable exceptions occurring at y/D = 0.6 (particularly for x/D = 6). At this radial station the skewness and kurtosis peak, reflecting the start of the somewhat abrupt transition from a relatively compact, Gaussian-like distribution to the strongly bi-modal pdf at the outer edges of the jet.

As a summary from the presentation of the pdfs, we find relatively quick changes in the mixing with radial distance around the shear layer and the passage of the vortex ring and we observe the effect of large scale mixing structures even at the centreline of the jet.

IV. INSTANTANEOUS AND MEAN SCALAR DISSIPATION RATE

The results of the scalar dissipation rate are presented in mm^{-2}, where, for isothermal conditions and temperature 20 °C, a diffusivity $\mathfrak{D} = 20$ mm^2/s can be assumed to obtain units of s^{-1}. Figure 13 shows instantaneous images of the logarithm of the scalar dissipation for some times after the start of injection. Each image is around 5 nozzle diameters wide (centred on the jet centerline) and, in the axial direction, is cropped to the axial penetration length of the jet at the given time. The instantaneous images have few common characteristics. For the times that the vortex ring has not pinched off the jet body, the scalar dissipation rate is high at the periphery of the jet. It forms a thin layer that follows the instantaneous jet contour and the larger structures that are formed due to

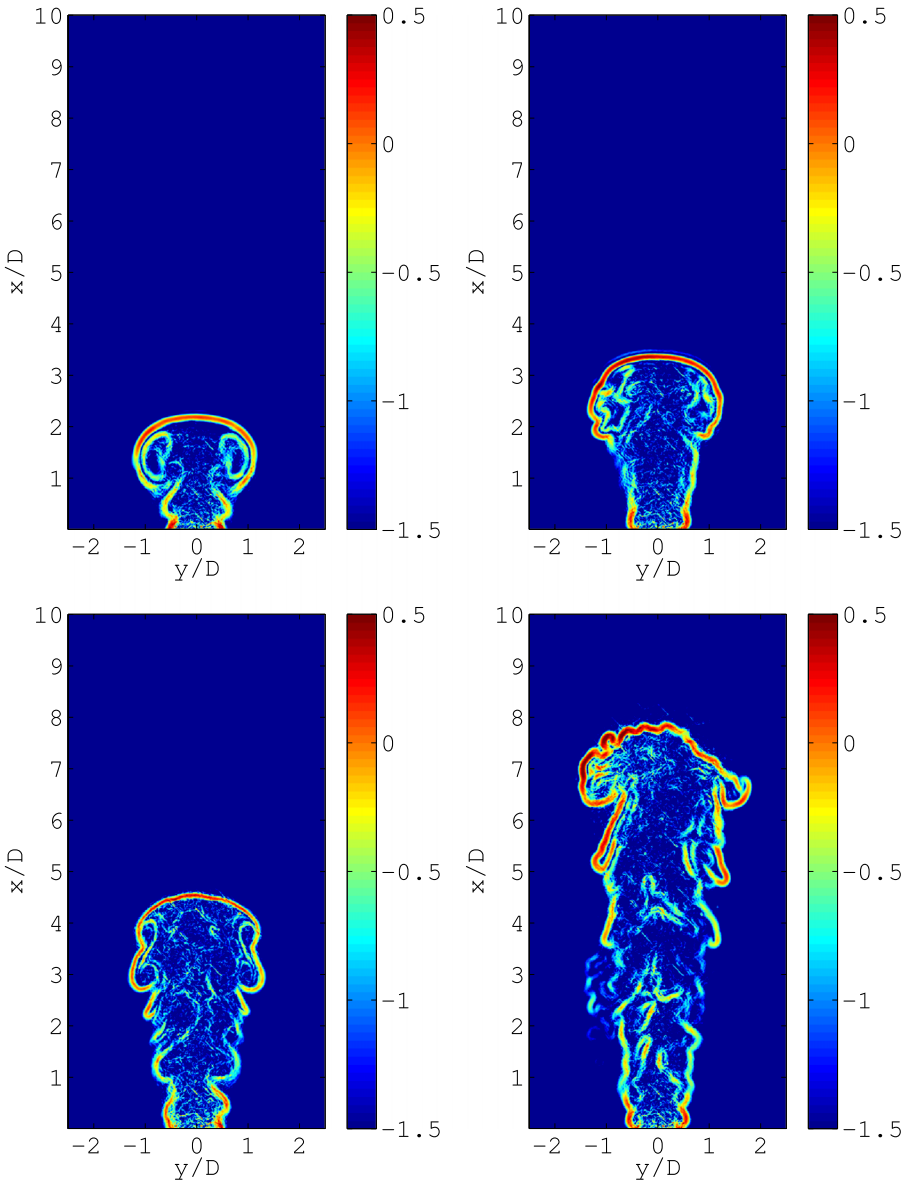

FIG. 13. Sample instantaneous images of the logarithm of the scalar dissipation rate (divided by the diffusivity) at various times after the start of injection. From left to right and top to bottom, t/T = 3.4, 7.15, 9.65 and 15.9. Note that, whereas the radial extent of each image is the same, the axial extent is different. The colour scale is the same for all images.

ambient fluid engulfment. At the same time, the highest scalar dissipation values are continuously present at the shear layer formed near the nozzle exit. This thin layer persists spatially from the jet nozzle exit to the head vortex in all instantaneous images for times until t/T ≈ 10. In contrast, inside the jet body the level of the dissipation rate is markedly smaller and, additionally, ordered structures with high dissipation appear only occasionally at the instantaneous images. This is more evident at the earlier times ASI, when high dissipation follows the large scale structures responsible for bringing ambient and jet fluids into contact. As there are more corrugations with increasing time and during the end of injection, only then do the dissipation layers become more apparent within the jet body. This description is slightly different to the picture in the far field of steady jets,[31,38] where the dissipation layers are intermittently present within the jet body.

Figure 14 shows the mean scalar dissipation at different times after the start of injection. The values of the scalar dissipation rate are generally smaller compared to the values in Figure 13 for

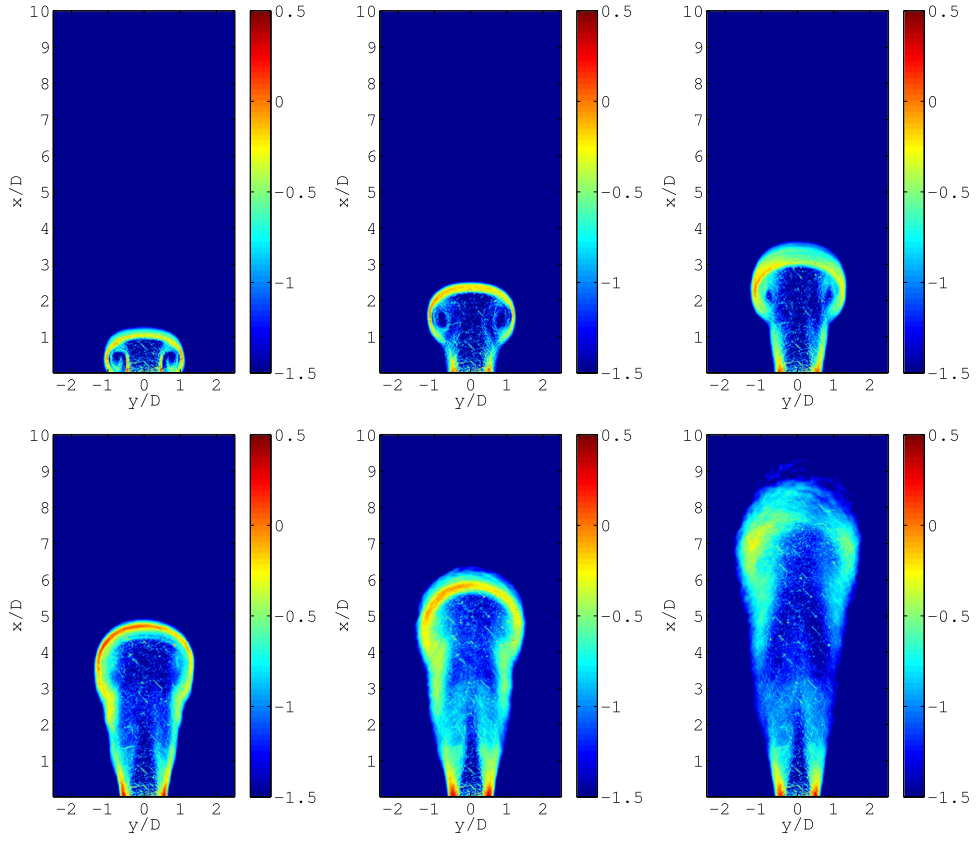

FIG. 14. Images of the logarithm of the mean scalar dissipation (over the diffusivity). The time after the start of injection is (from left to right and top to bottom) t/T = 2.15, 4.65, 7.15, 9.65, 13.4.

the instantaneous scalar dissipation. Whereas values of the scalar dissipation of more than 40 s^{-1} are typical at the instantaneous flow realisations, it is not common to find corresponding values larger than ~5 s^{-1} at the mean flow images. An exception is in the shear layer at the nozzle exit, where the mixture fraction gradients are the largest since there is no mixing and the jet fluid concentration changes from 1 to 0 within the short diffusion layer. Another observation is the absence of any particular structure of the scalar dissipation inside the jet body, apart from the vortex ring at the earlier times. During these times the structure of the vortex ring with the vortex core is still apparent and there is a noticeable change, at the vortex ring, in the development of the jet contour from the nozzle exit to downstream distances. At later times, until time t/T = 9.65, the width of the jet starts to follow a linear expansion with downstream distance, approaching the linear development pattern of a steady jet.

The scalar dissipation is, as in the instantaneous images, concentrated at the jet periphery and at the leading edge of the vortex ring. However, in the mean images, the layer that includes most of the dissipation and surrounds the jet is not as thin as it was in the instantaneous images. Both at the head vortex and at the shear layer around the main jet body a thick contour is formed. Part of the thickness of this contour, especially at the leading edge of the head vortex, is due to the differences in the instantaneous penetration distance between the various injections. Due to these differences, the very thin layer of each instantaneous realisation is not superimposed at a fixed axial distance with the corresponding layer of other flow realisations.

V. STATISTICAL MEASURES OF THE SCALAR DISSIPATION RATE

The probability density function of the scalar dissipation rate is an important quantity in the description and calculation of turbulent isothermal and reacting flows and, commonly, a log-normal

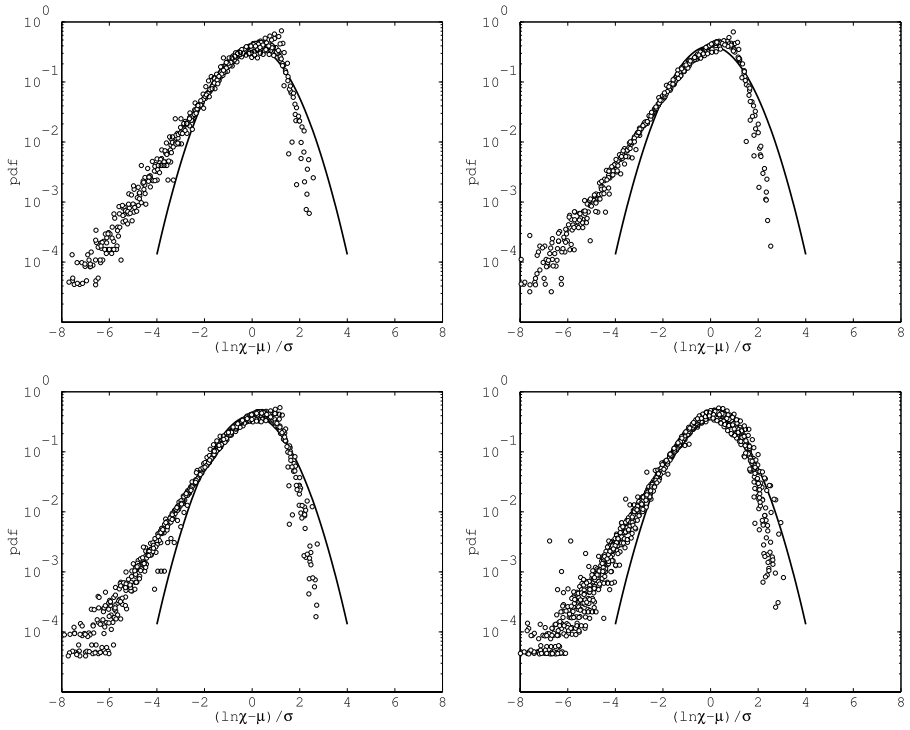

FIG. 15. The pdf of the normalised logarithm of the scalar dissipation rate for some times after the start of injection and various flow positions (all drawn using the same symbol). From left to right and top to bottom the times are t/T = 4.65, 5.9, 9.65, and 13.4. The solid line denotes the lognormal pdf.

pdf is used to characterise the distribution of dissipation rate values. Figure 15 shows the pdf of χ for various flow positions and times ASI. The pdf is normalised using the local mean and standard deviation values and shown in logarithmic axes, in which a log-normally distributed variable is a parabola. The pdf for all times ASI shown have some common characteristics, i.e., negative skewness and faster roll-off at large values, when compared to a lognormal distribution — this behaviour of the pdf has been widely observed in many isothermal and reacting flows. The difference between measured lognormal pdf, at low dissipation rate values, could potentially be attributed to effects, such as signal noise and measurement resolution, flow location or dimensionality of the measurements, or it could be an inherent feature of the dissipation rate pdf. The noise contribution and the resolution blurring to the measured scalar dissipation rate have been dealt with using a Wiener filter and, as in previous experiments,[31] artificial addition of noise and blurring does not provide conclusive evidence for the negative skewness of the pdf. With respect to the flow location, the pdfs are estimated by collecting measured values only when jet fluid is actually present in the measurement location, so it is unlikely to find a large proportion of low dissipation just by measuring in a region when only ambient fluid is present; additionally, collecting dissipation rate values where no jet fluid is present could lead to a bimodal dissipation pdf.[23] Finally, the dimensionality of the measurements has been assumed to contribute to the discrepancy between measured and lognormal pdf. Corrections to reconstruct the pdf that would be measured using all three components of the scalar gradient, assuming isotropy, point to a better fit to a lognormal.[33] In the present measurements, using one or two components of the gradient to calculate the dissipation rate, resulted in pdfs that are largely indistinguishable from each other; whether the full scalar gradient would alter this image is unclear. This is not only of theoretical importance, however, because in certain situations the low dissipation rate values are important in controlling a physical process (e.g., in auto-ignition).

Negatively skewed probability density functions similar to those in Figure 15 have also been observed in seemingly unrelated experiments measuring the fluctuations in the power consumption in a turbulent flow[39] and in the alignment of molecules in a liquid crystal,[40] among others. It is

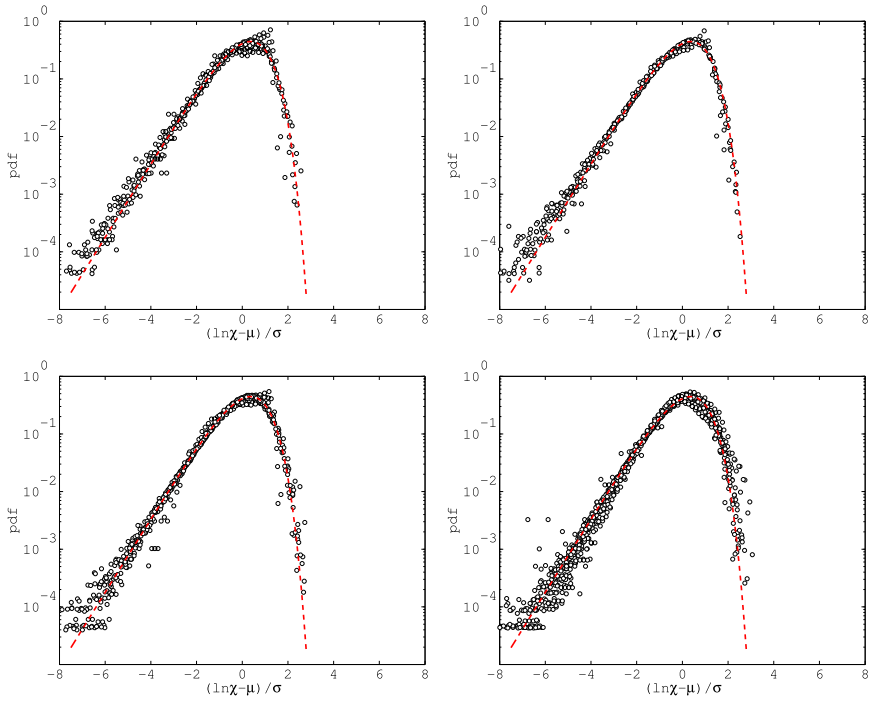

FIG. 16. The pdf of Figure 15 compared with the distribution of Equation (1).

suggested that these systems have in common a correlation length scale which is of the same order as the system size. To test this effect, we compare the experimental results with a pdf derived from the generalised Gumbel distribution, which has been shown to fit well such phenomena.[40] The form of the distribution for a normalised variable,[41] using the mean and the standard deviation, is

$$\Pi(\theta) = w \exp\{\alpha b(\theta - s) - \alpha \exp[b(\theta - s)]\}, \tag{1}$$

where the parameters are $\alpha = \pi/2$, $b = 0.938$, $s = 0.374$, and $w = 2.14$. Figure 16 redraws the pdf in Figure 15, this time compared with the Bramwell-Holdsworth-Pinton distribution (Equation (1)). The agreement between the measured data and assumed distribution is remarkable and it implies that finite size effects are important in this flow. In the present experiment, the large scale structures that drive the jet's development seem to produce long range correlations in the scalar dissipation rate (such as in Figure 13), perhaps due to the early stage development of the scalar turbulence in this flow.

A. Conditional statistics of the scalar dissipation rate

The conditional statistics of the scalar dissipation rate are important quantities in the description and modelling of turbulent reacting flows. Considering the auto-ignition of a diesel jet, a conceptual model of diesel engine combustion[42] points to the importance of the auto-ignition location to help control emissions of soot and NO_x; it is suggested that the equivalence ratio (ϕ; which measures, by mass, the excess fuel in relation to the stoichiometric condition) at which auto-ignition takes place is between 2 and 4 at a temperature of 800–1000 K. These conditions promote the production of soot (which oxidises later in the cycle) and the creation of NO_x in the ensuing high temperature stoichiometric diffusion flame. Controlling the initial level of premixing can help control the level of the resulting emissions. This qualitative description agrees with the notion of the "most reacting" mixture fraction,[43] ζ_{MR} – this is the value of the mixture fraction at which auto-ignition is most likely to occur. It has been found from chemical kinetic and fluid dynamic calculations that ζ_{MR} is generally different to the stoichiometric mixture fraction and depends on fuel and local temperature and pressure. At the same time, it has been observed that auto-ignition happens when ζ_{MR} is coupled with relatively low conditional scalar dissipation.

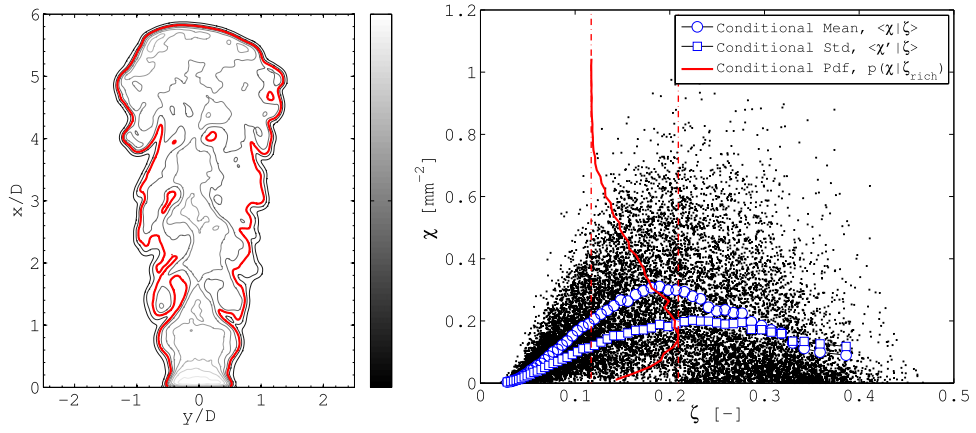

FIG. 17. The conditional statistics of scalar dissipation rate give the values of χ along a given contour, for example, the contour shown in the image on the left. We present the conditional statistics along a given contour as well as a specific spatial location. The graph on the right shows a scatter plot of mixture fraction and scalar dissipation rate values around (x/D,y/D) = (2,0.9) at time t/T = 6.95, where the values within the two vertical lines correspond to the dissipation along the given contour. Data are collected over an area $\Delta x * \Delta y \approx 4\eta_B * 3\eta_B$ around the spatial location and every 10th data point is plotted. Also shown are the conditional mean and standard deviation and the conditional pdf of the scalar dissipation rate for the given contour, $0.11 < \zeta_{rich} < 0.21$.

For example, the stoichiometric mixture fraction of n-heptane is $\zeta_{st} = 0.062$ and for conditions corresponding to diesel engines (i.e., oxidiser temperature 800 K and pressure 50 bar) it is found that[44–46] $\zeta_{MR} \approx 0.1$–0.3. At these conditions, an average value of the critical scalar dissipation rate for $2 < \phi < 4$ (alternatively,[47] $0.11 < \zeta_{rich} < 0.21$) is $\langle\chi|\zeta_{rich}\rangle_{cr} \sim 37\ s^{-1}$ found from laminar flamelet calculations.[48] This range of mixture fractions covers the rich mixture found in diesel engines prior to autoignition and at the same time accounts for the broad variation of ζ_{MR} as typically observed. Additionally, the critical conditional scalar dissipation rate at the stoichiometric mixture fraction is[44] $\langle\chi|\zeta_{st}\rangle_{cr} \sim 10\ s^{-1}$. In order to obtain the gradients of the mixture fraction and compare with the present results, a diffusivity $D = 110\ mm^2/s$ is used (corresponding to the conditions near top dead centre), giving $\langle\chi|\zeta_{st}\rangle_{cr} \sim 0.09\ mm^{-2}$, and $\langle\chi|\zeta_{rich}\rangle_{cr} \sim 0.34\ mm^{-2}$.

The conditional statistics of the scalar dissipation rate are defined by reference to Figure 17, which shows a scatter plot of mixture fraction/scalar dissipation data for a given spatial location and a single time ASI, gathered over all the instantaneous images; the extent of the spatial location is $\Delta x * \Delta y \approx 4\eta_B * 3\eta_B$. The range of the local mixture fraction values is divided into a number of bins, with 2000–4000 values in each one, and the conditional mean, $\langle\chi|\zeta\rangle$, and conditional standard deviation, $\langle\chi'|\zeta\rangle$, of scalar dissipation are calculated from the values at each mixture fraction bin. In addition, the conditional pdf of $\chi|\zeta$, $p(\chi|\zeta)$, for a range of mixture fraction values, is calculated from the values within the two vertical lines.

Some examples of the mean conditional scalar dissipation rate are shown in Figures 18-20, where each plot shows the conditional dissipation profiles for various radial distances, at the same axial distance and at the same time ASI. At all positions and at all times ASI, the conditional profiles cover various ranges of mixture fraction values, due to the difference range covered by

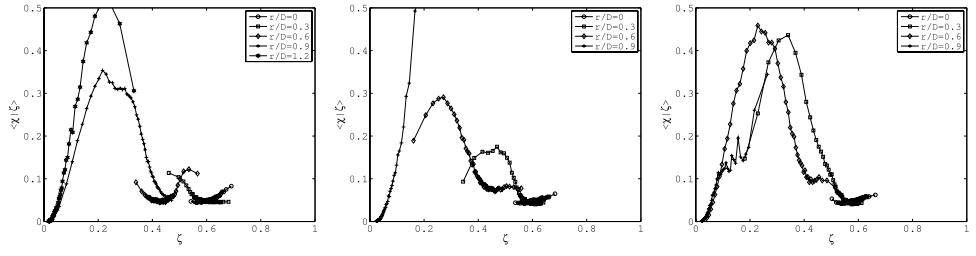

FIG. 18. Mean conditional scalar dissipation rate at x/D = 1. From left to right, the time ASI is t/T = 4.65, 7.15 and 10.9.

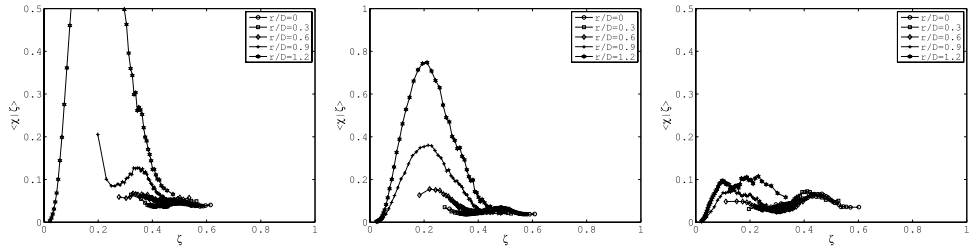

FIG. 19. Mean conditional scalar dissipation rate at x/D = 4. From left to right, the time ASI is t/T = 9.65, 10.9 and 13.4.

the local pdf of mixture fraction. With increasing time ASI and distance from the nozzle exit, due to entrainment of ambient air the range of ζ values covered by the conditional profiles becomes similar between various radial positions. At x/D = 1 and just after the start of injection, the mean conditional dissipation is small inside the jet body, for r/D $\leq$0.6, and relatively constant across the mixture fraction range, given that limited mixing has taken place. Very large values of the mean conditional dissipation are found at the shear layer of the jet, for all times ASI; however, with increasing time ASI the mean conditional dissipation is of comparable magnitude at all radial positions. At x/D = 4, the mean conditional dissipation is small and relatively constant inside the jet body, rising fast at the shear layer, similarly to x/D = 1. Also, as the time ASI progresses, the values of the conditional dissipation become of comparable magnitude. In contrast, though, to the more upstream position, and with increasing time ASI, the largest values of the conditional dissipation (at the shear layer) reduce, to become comparable to the dissipation values within the jet body. We note, also, that the peak values of the mean conditional dissipation at x/D = 1, for the later times ASI, are always larger than the values at x/D = 4 ($\langle\chi|\zeta\rangle > 0.2$ mm^{-2} compared to ($\chi|\zeta\rangle < 0.1$ mm^{-2}) and that there is a variation of the values across the mixture fraction range, whereas at x/D = 4 the profiles are rather constant. At the most downstream position x/D = 8, Figure 20, the conditional dissipation has the same magnitude at any given time ASI, irrespective of the radial position. For later times the conditional dissipation relaxes to lower values, comparable to the ones at x/D = 4, and the profiles become rather constant across the mixture fraction range.

The largest values of the dissipation conditional on the stoichiometric mixture fraction are always found near the nozzle exit, between x/D = 1 and x/D = 2, and are generally lower than the critical dissipation value at stoichiometric conditions, Figure 21. The radial profiles of $\langle\chi|\zeta_{st}\rangle$ peak around y/D = 0.9 for most of the times after the start of injection and for nearly all the downstream distances from the nozzle exit. With increasing time, the profiles become flatter for positions around the shear layer and extend further outwards in the radial direction, up to y/D = 1.2; at the later times they tend to assume a flat form around the shear layer with relatively low dissipation values, about half the critical value. However, the conditional fluctuations can be as large as 100% of the mean at these conditions. The spatial gradients of these profiles can be quite large for the earlier times after the start of injection, so it might not be possible to use a single form to describe the conditional profiles for all times ASI.

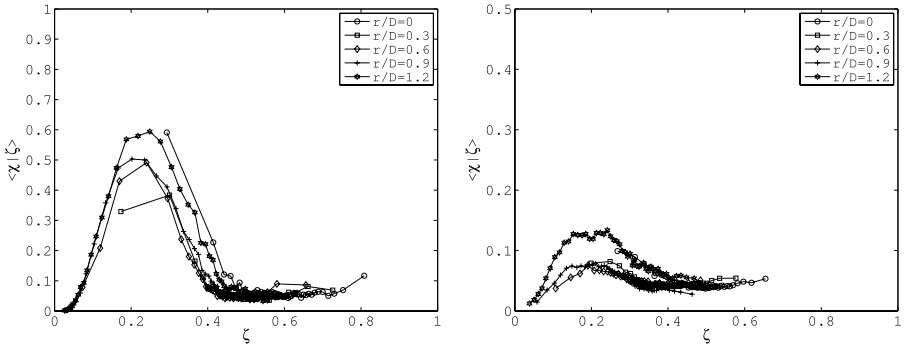

FIG. 20. Mean conditional scalar dissipation rate at x/D = 8. From left to right, the time ASI is t/T = 13.4 and 15.9.

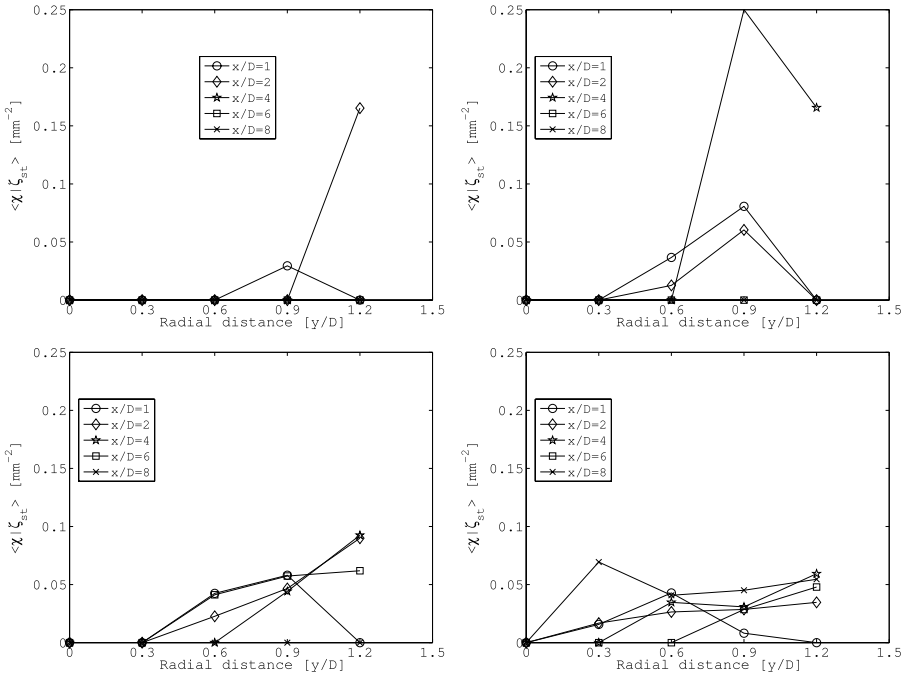

FIG. 21. The mean scalar dissipation rate conditional on the stoichiometric value of the mixture fraction, as a function of the radial distance. The times after the start of injection are (from left to right and top to bottom) t/T = 5.9, 9.6, 10.9, and 13.4.

The radial profiles of the scalar dissipation conditioned on rich mixture fraction, Figure 22, reach further inside the jet body compared with the stoichiometric conditional profiles, since the rich mean mixture fraction contours are physically situated closer to the jet centreline. The change in the conditional values with radial distance is apparent in this case as in the stoichiometric

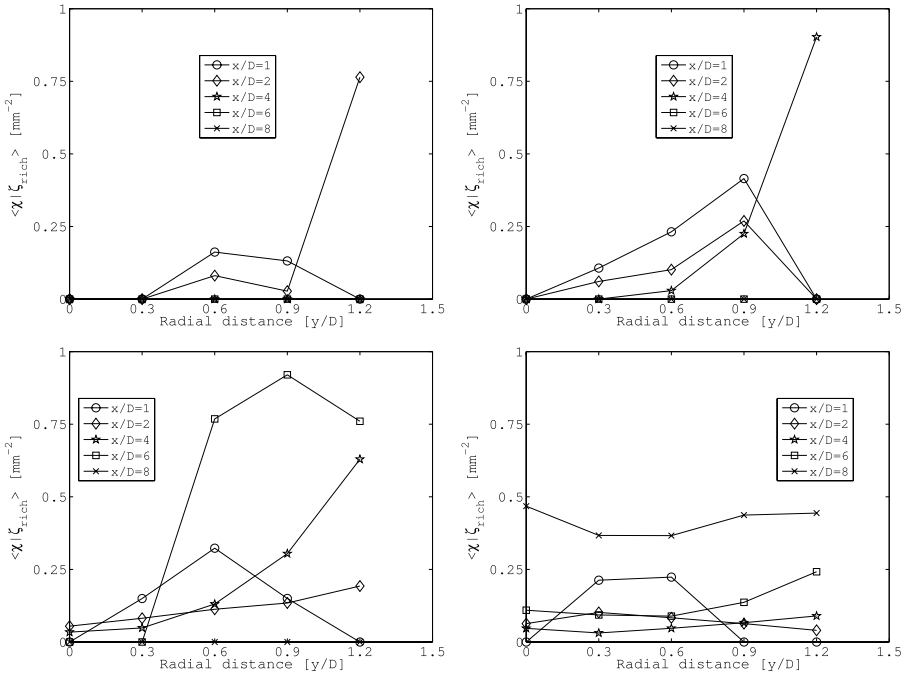

FIG. 22. The mean scalar dissipation rate conditional on rich values of the mixture fraction, as a function of the radial distance. The times after the start of injection are (from left to right and top to bottom) t/T = 5.9, 9.6, 10.9, and 13.4.

conditional profiles. The relevant peak in the radial direction is around y/D = 0.9 at the earlier times, similar to the profiles in Figure 21 and moves closer to the centreline, around y/D = 0.6, at later times after the start of injection. With increasing time and downstream distance, appreciable values of the conditional dissipation rate appear even on the jet centreline. It is also the case with the rich conditional profiles, as with the stoichiometric ones, that the largest values of the conditional dissipation are found at the near nozzle positions, x/D = 1 to x/D = 4, for all times after the start of injection. With increasing time, the radial profiles for almost all downstream distances flatten out, however, the level of the conditional dissipation varies between downstream distances. At the last time shown in Figure 22, t/T = 13.4, and from x/D = 2 to x/D = 6 the rich conditional dissipation values have similar magnitude across the jet. The absolute values of $\langle \chi | \zeta_{\text{rich}} \rangle$ are generally much larger than $\langle \chi | \zeta_{\text{st}} \rangle$ and in some cases even an order of magnitude larger. As compared to the critical dissipation, the values of the rich conditional dissipation are generally lower and at later times about a third of the critical value, with the exception of the near nozzle positions, where they are of comparable magnitude, and the vortex ring positions (e.g., the x/D = 8 curve at t/T = 13.4 in Figure 22) where they exceed the critical dissipation. In the rich conditional profiles as well, the conditional fluctuations tend to increase with time reaching again about 100% of the mean, as in the stoichiometric conditional dissipation. However, as an example and in contrast to the stoichiometric conditional profiles, it would take three standard deviations to reach and exceed the critical dissipation value, say at t/T = 13.4 for x/D = 2 to x/D = 6 in Figure 21. So, comparing Figures 21 and 22, for the estimated critical dissipation values, $\langle \chi | \zeta_{\text{st}} \rangle$ is generally below the critical value, whereas $\langle \chi | \zeta_{\text{rich}} \rangle$ can be either lower or higher than the critical value depending on spatial location in the flow and time after the start of injection.

The results of Figures 21 and 22 present the mean conditional dissipation rate and compare that with estimated (auto-)ignition critical values, but the distributions of the conditional scalar dissipation rate are, also, important. Figure 23 shows the normalised pdf of the logarithm of the conditional scalar dissipation rate at rich mixture conditions (i.e., the pdf of the quantity

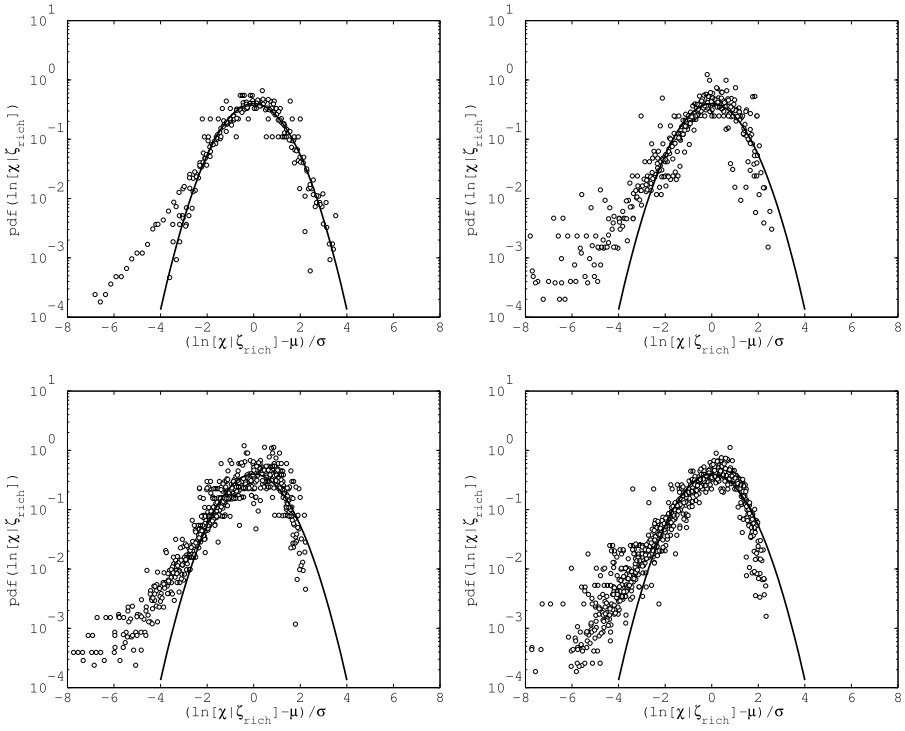

FIG. 23. The pdf of the logarithm of the scalar dissipation rate conditional on rich values of the mixture fraction. The pdf at various spatial locations are shown in symbols and the solid line is a log-normal distribution; μ and σ are the mean and the standard deviation of $\ln(\chi|\zeta_{\text{rich}})$, respectively. The times after the start of injection are (from left to right and top to bottom) t/T = 5.9, 9.6, 10.9, 13.4.

$[\ln(\chi|\zeta_{\text{rich}}) - \mu]/\sigma$, where μ and σ are the mean value and the standard deviation of $\ln(\chi|\zeta_{\text{rich}})$, respectively); each plot collects the pdf for various spatial locations at each time instant and compares those with a log-normal distribution. As in the case of the unconditional pdf of χ, the assumption of log-normality only partially does it hold for most cases (spatial locations and times after the start of injection), except for few pdf at the earliest time shown (t/T = 5.9). The estimated pdf can be described adequately by the assumed log-normal form in a range of ±2 standard deviations from the mean. In contrast, a mismatch is seen at both lower and higher dissipation values, where at the high end of the distributions the estimated pdf show a steeper fall off than a lognormal distribution, albeit less steep than in the case of the unconditional pdf. The departure from log-normality is accentuated for lower dissipation values and this might be important, since the lower values of the scalar dissipation are more relevant in allowing (auto-)ignition. The characteristics of the conditional dissipation pdf have been observed for both the unconditional and conditional pdf at various flow configurations and Reynolds numbers.

Each of the conditional pdf was collected for a given spatial location and constant time after the start of injection and show that the normalised pdf at different positions and times are similar. Since there is a large variation of conditional scalar dissipation values and given that a persistence of small conditional dissipation is advantageous for (auto-)ignition, it is instructive, to follow the time variation of the conditional mean and standard deviation of the scalar dissipation. Figure 24 shows the time variation of the mean conditional dissipation at various locations in the flow and Figure 25 shows the time variation of the conditional standard deviation. At the mean conditional dissipation plots the passage of the vortex ring is manifested from the large spike in the scalar dissipation rate. With increasing time the conditional dissipation falls quite fast and, at the later times shown, it tends to assume a somehow constant, and rather low, value, irrespective of spatial location in the flow. Closer to the nozzle, the convergence of the conditional mean dissipation values is slower than further downstream (cf. Figure 22) and in all cases a constant value is achieved after t/T ∼ 15. So, upstream of the vortex ring and across the jet, the conditional mean of the scalar dissipation is low; however, it takes some time, 3–5 T, for the values to equilibrate. This implies that just after the passage of the vortex ring the history of the conditional mean dissipation is not favourable

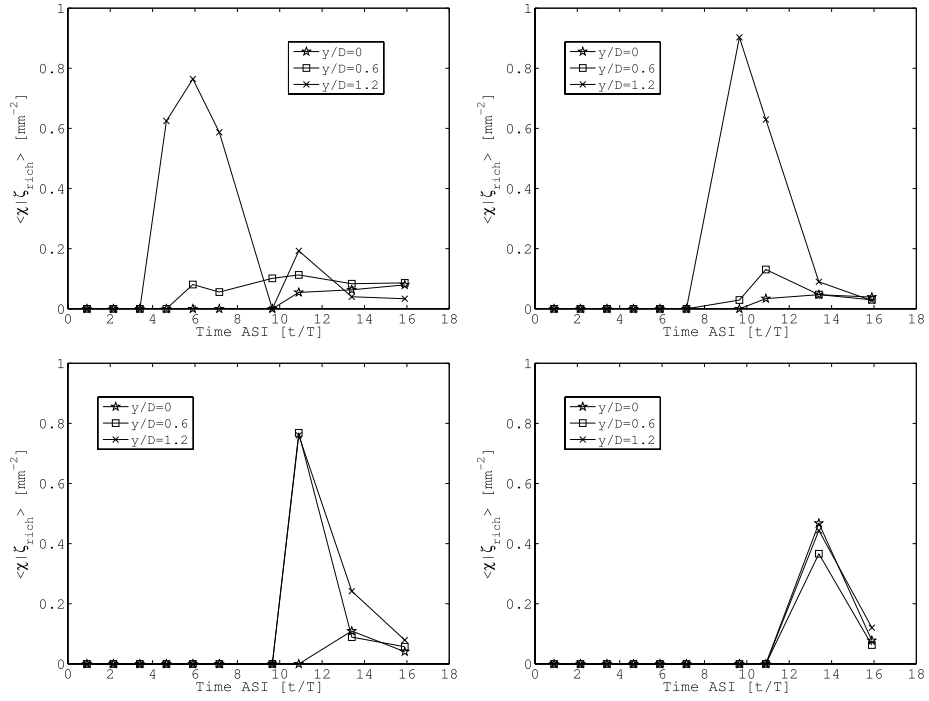

FIG. 24. The temporal variation of the mean scalar dissipation rate conditional on rich values of the mixture fraction. The downstream distances are (from left to right and top to bottom) x/D = 2, 4, 6, 8.

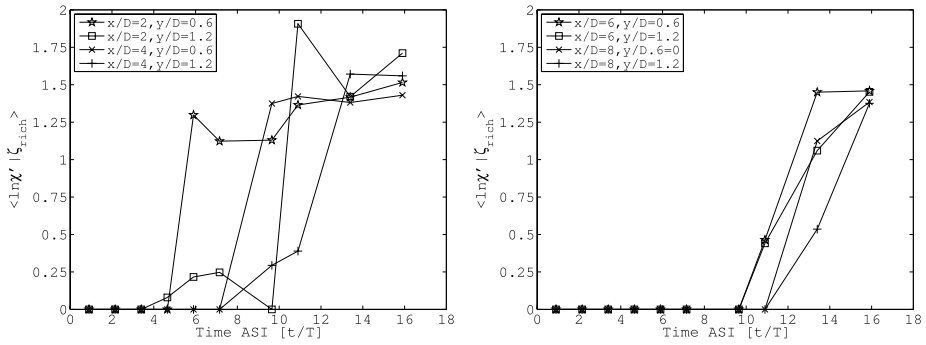

FIG. 25. The temporal variation of the standard deviation of the scalar dissipation rate conditional on rich values of the mixture fraction. The two graphs show different downstream distances for clarity.

for auto-ignition, in the sense that consistently low dissipations are rather slow to achieve. The conditional standard deviation of the logarithm of the scalar dissipation, Figure 25, shows that the conditional fluctuations around the mean value reach a constant value at a comparable delay after the passage of the vortex ring as the conditional mean (~5 T), and reach similar values at all spatial locations in the flow. The observation of constant standard deviation at later times might be advantageous when trying to predict the variation of the conditional dissipation. However, at earlier times the conditional fluctuations differ for different flow locations. Compared to the critical conditional dissipation value, the measured values close to the nozzle exit (for x/D < 2) are always larger, implying an unfavourable condition for auto-ignition. A similar picture seems to hold true for locations at the leading edge and at the vortex ring. Identifying the vortex ring at the edges of the jet, at roughly y/D = 1.2, Figure 24 shows that these values are also larger than the critical value, until some time after the passage of the vortex ring — this time "delay" seems to be similar for all downstream distances, being t/T ~ 4.

Finally, Figure 26 shows the ratio of the conditional standard deviation to the conditional mean, which is often assumed to have a constant value (values between 1 and 2 are typically used). The results show that this ratio seems to converge to a constant value of around 1.4 for downstream distances nearer the nozzle exit, irrespective of the radial position in the flow; measured values in the literature range from 1.2 to 1.31 for steady jets.[32,49] Further downstream, the ratio is 1–1.2, but still increases with time; whether the ratio will equilibrate at the same value at times past the latest time measured is unclear. The interesting point, however, is that the ratio varies in time, so it does not attain the final value immediately, but it does so some time after the passage of the vortex ring, with this time being longer at further distances from the nozzle exit.

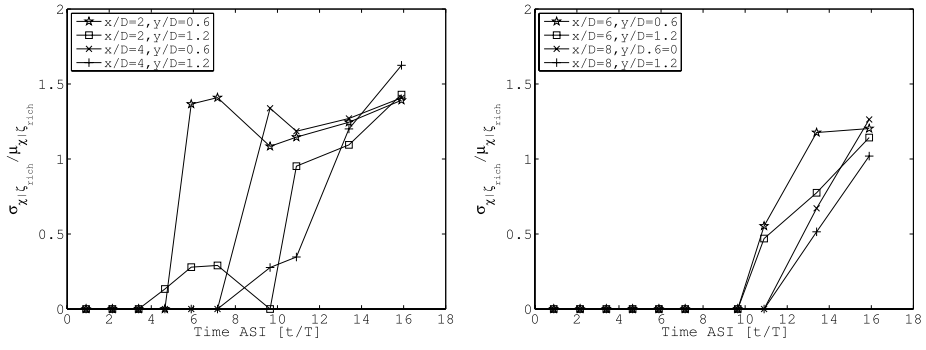

FIG. 26. The temporal variation of the ratio of the conditional standard deviation over the conditional mean of the scalar dissipation rate; conditioning is on the rich mixture fractions. The two graphs show different downstream distances for clarity.

VI. SUMMARY

An experiment of a starting gas jet was used to quantify large- and small-scale mixing, using the mixture fraction of the isothermal starting jet and its scalar dissipation rate. The development of the flow field is dominated at early times ASI by the induced vortex ring, whose effect becomes less prominent at later times ASI; once the vortex ring pinches-off the main jet body, the upstream jet resembles a quasi-steady jet. The pdf of the mixture fraction revealed the large scale intermittency found at the shear layer of the jet, and, also, the effect of large structures in bringing ambient fluid almost at the jet centreline, for both early and late times ASI. Other than at specific spatial locations, near the centreline or just inside the shear layer depending on time ASI, the mixture fraction pdfs were broad, skewed and, on occasion, bimodal.

The highest scalar dissipation rate was found at the periphery of the jet and at the leading edge, for all times ASI. Within the jet body the scalar dissipation attained lower values and only at later times ASI were there large dissipation values and the characteristic dissipation layers. The pdfs of the scalar dissipation rate were negatively skewed, with the skewness reducing with increasing time ASI — at the large dissipation values, the pdfs were steeper than a lognormal distribution, becoming smoother with increasing time ASI. Similar observations hold, also, for the conditional pdf of the scalar dissipation. The mean conditional dissipation depends on the flow location and the underlying scalar pdf, more so for earlier times ASI than later after the injection, and the form of the conditional profiles becomes similar for various spatial locations only late after the injection. Finally, the conditional mean (and standard deviation) attain relatively constant values only after the passage of the vortex ring from a particular location (more prominently for the mean than the standard deviation) and, consequently, it maintains relatively low values of the dissipation, i.e., lower than an estimated critical value. The scalar dissipation conditional on mixture fraction between 0.11 and 0.21 can be as high as 0.9 mm^{-2} and following the passage of the vortex ring it can attain values less than 0.1 mm^{-2}, compared to a critical value for auto-ignition of ~0.35 mm^{-2}. The implications for auto-ignition rest on the time variation of these values and the spatial location where these are attained.

ACKNOWLEDGMENTS

The authors would like to acknowledge financial support from EPRSC Grant Nos. GR/R54767/01 and EP/G01597X/1.

[1] D. I. Pullin, "Vortex ring formation at tube and orifice openings," Phys. Fluids (1958-1988) **22**, 401–403 (1979).
[2] J. S. Turner, "The 'starting plume' in neutral surroundings," J. Fluid Mech. **13**, 356–368 (1962).
[3] P. Witze, "The impulsively started incompressible tubrulent jet," Technical Report SAND80-8617, Sandia Laboratories, 1980.
[4] G. Cossali, A. Coghe, and L. Araneo, "Near-field entrainment in an impulsively started turbulent gas jet," AIAA J. **39**, 1113–1122 (2001).
[5] I. Immaculada, V. Marcos, L. S. Antonio, and L. Amable, "Simulations of starting gas jets at low Mach numbers," Phys. Fluids **17**, 038105 (2005).
[6] G. E. Cossali, "An integral model for gas entrainment into full cone sprays," J. Fluid Mech. **439**, 353–366 (2001).
[7] R. Andriani, A. Coghe, and G. Cossali, "Near-field entrainment in unsteady gas jets and diesel sprays: A comparative study," Symp. (Int.) Combust. **26**, 2549–2556 (1996).
[8] F. Lahbabi, J. Borée, H. Nuglisch, and G. Charnay, "Anaylsis of starting and steady turbulent jets by image processing techniques," in *ASME, Experimental and Numerical Flow Visualization* (ASME, 1993), Vol. 172, pp. 315–321.
[9] M. Gharib, E. Rambod, and K. Shariff, "A universal time scale for vortex ring formation," J. Fluid Mech. **360**, 121–140 (1998).
[10] R. Sau and K. Mahesh, "Passive scalar mixing in vortex rings," J. Fluid Mech. **582**, 449–461 (2007).
[11] K. R. Sreenivasan, "On local isotropy of passive scalars in turbulent shear flows," Proc. R. Soc. A **434**, 165–182 (1991).
[12] N. Peters, *Turbulent Combustion* (Cambridge University Press, 2000).
[13] Z. Warhaft, "Passive scalars in turbulent flows," Annu. Rev. Fluid Mech. **32**, 203–240 (2000).
[14] R. Bilger, "Some aspects of scalar dissipation," Flow, Turbul. Combust. **72**, 93–104 (2004).
[15] F. Anselmet, H. Djeridi, and L. Fulachier, "Joint statistics of a passive scalar and its dissipation in turbulent flows," J. Fluid Mech. **280**, 173–197 (1994).
[16] F. Gao and E. E. O'Brien, "Joint probability density function of a scalar and its gradient in isotropic turbulence," Phys. Fluids **3**, 1625–1632 (1991).
[17] K. Sardi, A. M. K. P. Taylor, and J. H. Whitelaw, "Conditional scalar dissipation statistics in a turbulent counterflow," J. Fluid Mech. **361**, 1–24 (1998).

[18] V. Eswaran and S. B. Pope, "Direct numerical simulations of the turbulent mixing of a passive scalar," Phys. Fluids (1958-1988) **31**, 506–520 (1988).
[19] Jayesh and Z. Warhaft, "Probability distribution of a passive scalar in grid-generated turbulence," Phys. Rev. Lett. **67**, 3503–3506 (1991).
[20] Jayesh and Z. Warhaft, "Probability distribution, conditional dissipation and transport of passive temperature flucuations in grid-generated turbulence," Phys. Fluids **4**, 2292–2307 (1992).
[21] P. Kailasnath, K. R. Sreenivasan, and J. Saylor, "Conditional scalar dissipation rates in turbulent wakes, jets and boundary layers," Phys. Fluids **5**, 3207–3215 (1993).
[22] J. Mi, R. Antonia, and F. Anselmet, "Joint statistics between temperature and its dissipation rate components in a round jet," Phys. Fluids **7**, 1665–1673 (1995).
[23] W. M. Pitts, C. D. Richards, and M. S. Levenson, "Large – and small – scale structures and their interaction in an axisymmetric jet," Technical Report NISTIR 6393, National Institute of Standards and Technology, 1999.
[24] D. Geyer, A. Kempf, A. Dreizler, and J. Janicka, "Scalar dissipation rates in isothermal and reactive opposed jets: 1–D–Raman/Rayleigh experiments supported by LES," Proc. Combust. Inst. **30**, 681–689 (2005).
[25] E. S. C. Ching and Y. K. Tsang, "Passive scalar conditional statistics in a model random advection," Phys. Fluids **9**, 1353–1361 (1997).
[26] J. B. Kelman and A. R. Masri, "Reaction zone structure and scalar dissipation rates in turbulent diffusion flames," Combust. Sci. Technol. **129**, 17–55 (1997).
[27] S. H. Stårner, R. W. Bilger, M. B. Long, J. H. Frank, and D. F. Marran, "Scalar dissipation measurements in turbulent jet diffusion flames of air diluted methane and hydrogen," Combust. Sci. Technol. **129**, 141–163 (1997).
[28] A. N. Karpetis and R. S. Barlow, "Measurements of scalar dissipation in a turbulent piloted methane/air jet flame," Proc. Combust. Inst. **29**, 1929–1936 (2002).
[29] J. A. Sutton and J. F. Driscoll, "Measurements and statistics of mixture fraction and scalar dissipation rates in turbulent non-premixed jet flames," Combust. Flame **160**, 1767–1778 (2013).
[30] D. Dowling, "The estimated scalar dissipation in gas-phase turbulent jets," Phys. Fluids A **3**, 2229–2246 (1991).
[31] L. K. Su and N. T. Clemens, "The structure of fine-scale scalar mixing in gas-phase planar turbulent jets," J. Fluid Mech. **488**, 1–29 (2003).
[32] C. Markides and E. Mastorakos, "Measurements of the statistical distribution of the scalar dissipation rate in turbulent axisymmetric plumes," Flow, Turbul. Combust. **81**, 221–234 (2008).
[33] W. Dahm and K. Buch, "Lognormality of the scalar dissipation PDF in turbulent flows," Phys. Fluids **1**, 1290–1293 (1989).
[34] J. W. Goodman, *Introduction to Fourier Optics*, 2nd ed. (McGraw–Hill International Editions, 1996).
[35] G.-H. Wang, A. Karpetis, and R. Barlow, "Dissipation length scales in turbulent nonpremixed jet flames," Combust. Flame **148**, 62–75 (2007).
[36] N. Soulopoulos, Y. Hardalupas, and A. M. K. P. Taylor, "Scalar dissipation rate measurements in a starting jet," Exp. Fluids **55**, 1–20 (2014).
[37] S. Abramovich and A. Solan, "The initial development of a submerged laminar round jet," J. Fluid Mech. **59**, 791–801 (1973).
[38] K. A. Buch and W. J. A. Dahm, "Experimental study of the fine scale structure of conserved scalar mixing in turbulent shear flows. Part 2. Sc ≈1," J. Fluid Mech. **364**, 1–29 (1998).
[39] S. T. Bramwell, P. C. W. Holdsworth, and J. F. Pinton, "Universality of rare fluctuations in turbulence and critical phenomena," Nature **396**, 552–554 (1998).
[40] S. Joubaud, A. Petrosyan, S. Ciliberto, and N. B. Garnier, "Experimental evidence of non-Gaussian fluctuations near a critical point," Phys. Rev. Lett. **100**, 180601 (2008).
[41] S. T. Bramwell, J. Y. Fortin, P. C. W. Holdsworth, S. Peysson, J. F. Pinton, B. Portelli, and M. Sellitto, "Magnetic fluctuations in the classical XY model: The origin of an exponential tail in a complex system," Phys. Rev. E **63**, 041106 (2001).
[42] J. E. Dec, "A concenptual model of DI diesel combiustion based on laser-sheet imaging," SAE Technical Report No. 970873, 1997.
[43] E. Mastorakos, T. A. Baritaud, and T. J. Poinsot, "Numerical simulations of autoignition in turbulent mixing flows," Combust. Flame **109**, 198–223 (1997).
[44] H. Barths, H. Pitsch, and N. Peters, "3D simulation of DI diesel combustion and pollutant formation using a two-component reference fuel," Oil Gas Sci. Technol. **54**, 233–244 (1999).
[45] A. Viggiano and V. Magi, "A 2-D investigation of n-heptane autoignition by means of direct numerical simulation," Combust. Flame **137**, 432–443 (2004).
[46] A. Viggiano, "Exploring the effect of fluid dynamics and kinetic mechanisms on n-heptane autoignition in transient jets," Combust. Flame **157**, 328–340 (2010).
[47] The correspondence between mixture fraction and equivalence ratio is given by[12] $\phi = \frac{\zeta}{1-\zeta}\frac{1-\zeta_{st}}{\zeta_{st}}$.
[48] E. Mastorakos, "Ignition of turbulent non-premixed flames," Prog. Energy Combust. Sci. **35**, 57–97 (2009).
[49] E. Effelsberg and N. Peters, "Scalr dissipation in turbulent jets and jet diffusion flames," Symp. (Int.) Combust **22**, 693–700 (1989).